



**A COMPARISON OF EXPERIMENTAL AND THEORETICALLY
PREDICTED PRESSURE DISTRIBUTIONS AND FORCE AND
STABILITY COEFFICIENTS FOR A SPHERICALLY BLUNTED
CONE AT $M_{\infty} \sim 18$ AND ANGLES OF ATTACK**

Eugene C. Knox and Clark H. Lewis

ARO, Inc.

February 1966

Distribution of this document is unlimited.

**VON KÁRMÁN GAS DYNAMICS FACILITY
ARNOLD ENGINEERING DEVELOPMENT CENTER
AIR FORCE SYSTEMS COMMAND
ARNOLD AIR FORCE STATION, TENNESSEE**

NOTICES

When U. S. Government drawings specifications, or other data are used for any purpose other than a definitely related Government procurement operation, the Government thereby incurs no responsibility nor any obligation whatsoever, and the fact that the Government may have formulated, furnished, or in any way supplied the said drawings, specifications, or other data, is not to be regarded by implication or otherwise, or in any manner licensing the holder or any other person or corporation, or conveying any rights or permission to manufacture, use, or sell any patented invention that may in any way be related thereto.

Qualified users may obtain copies of this report from the Defense Documentation Center.

References to named commercial products in this report are not to be considered in any sense as an endorsement of the product by the United States Air Force or the Government.

A COMPARISON OF EXPERIMENTAL AND THEORETICALLY
PREDICTED PRESSURE DISTRIBUTIONS AND FORCE AND
STABILITY COEFFICIENTS FOR A SPHERICALLY BLUNTED
CONE AT $M_\infty \sim 18$ AND ANGLES OF ATTACK

Eugene C. Knox and Clark H. Lewis
ARO, Inc.

FOREWORD

The work reported herein was sponsored by the Arnold Engineering Development Center (AEDC), Air Force Systems Command (AFSC) under Program Element 62405334, Project 8953, Task 895303.

The results of the research presented were obtained by ARO, Inc. (a subsidiary of Sverdrup and Parcel, Inc.), contract operator of AEDC, AFSC, Arnold Air Force Station, Tennessee, under Contract AF 40(600)-1200. The analytical research was conducted under ARO Project No. VW3507, and the manuscript was submitted for publication on October 19, 1965.

Part of the work described herein was presented by the first author as a Master of Science thesis to the Virginia Polytechnic Institute, Blacksburg, Virginia.

The authors wish to acknowledge the assistance of Messrs. Lloyd Johnson and Billy Z. Jenkins, Army Missile Command, Redstone Arsenal, Alabama in developing the General Applied Sciences Laboratory (GASL) three-dimensional characteristics program into an operationally useful machine program and for their cooperation in providing many of the numerical solutions presented herein.

The authors also wish to acknowledge the assistance of Mr. Jack F. Roberts, ARO, Inc., for providing some previously unpublished experimental data and Mr. Marvin R. Reed, ARO, Inc., for developing the pressure interpolation and force coefficient machine programs.

This technical report has been reviewed and is approved.

Larry R. Walter
1/Lt, USAF
Gas Dynamics Division
DCS/Research

Donald R. Eastman, Jr.
DCS/Research

ABSTRACT

Analysis of experimental pressure distributions and force and moment coefficients for a 9-deg half-angle spherically blunted cone at $M_\infty \sim 18$ and $\alpha = 0$ to 20 deg is presented based on an ideal gas ($\gamma = 1.4$) three-dimensional characteristics solution developed by General Applied Sciences Laboratory (GASL). Comparisons are also made with predictions based on modified Newtonian theory. Pressure distributions along the windward and leeward streamlines were well predicted by the results from the GASL program at $\alpha \approx 10$ deg. For $\alpha < 10$ deg, comparison with the experimental data indicated differences attributed to viscous effects. For $\alpha > 10$ deg the numerical results were affected by necessary program modifications on the leeward side. Radial pressure distributions along the body surface from the GASL results showed the development of low pressure "wells" in the leeward region at $\alpha \geq 10$ deg. Similar distributions along a constant entropy surface within the inviscid shock layer indicated substantial delay in the formation of the low pressure "wells". C_N and C_m were found to be in good agreement with the experimental data when based on the GASL surface pressure distribution. Predicted values of C_A were about 40 percent below the experimental data over the entire range, $\alpha = 0$ to 20 deg, in agreement with a previous Newtonian based analysis. The difference is attributed to the viscous-induced drag increment. Computed slopes, C_{N_α} and C_{m_α} , were found to be well predicted by the integrated GASL results, whereas the modified Newtonian prediction was in poorer agreement with the trends of the experimental data.

CONTENTS

	<u>Page</u>
ABSTRACT	iii
NOMENCLATURE	vi
I. INTRODUCTION	1
II. INVESTIGATION	
2.1 Theoretical Considerations	2
2.2 Experimental Studies	4
III. RESULTS AND DISCUSSION	
3.1 Zero-Lift Pressure Distributions	5
3.2 Surface Pressure Distributions at Angles of Attack . .	6
3.3 Pressure and Streamline Distributions on a Constant Entropy Surface	11
3.4 Force and Moment Coefficients	13
IV. CONCLUDING REMARKS	15
APPENDIX - Force and Moment Equations	19
REFERENCES	24

ILLUSTRATIONS

Figure

1. Cone Nomenclature and Coordinate Systems	27
2. Zero-Lift Pressure Distribution over 9-deg Half-Angle Spherically Blunted Cones	28
3. Effects of Changes-of-Frame on Body Pressures at $\alpha = 10 \text{ deg}$	29
4. Scheduled Changes-of-Frame for Various Angles of Attack	31
5. Pressure Distributions along Most Windward and Leeward Streamlines at $M_\infty \sim 18$ and at Angles of Attack	32
6. Radial Pressure Distributions over a 9-deg Half-Angle Spherically Blunted Cone at $M_\infty \sim 18$ and $\alpha = 5 \text{ deg}$	35
7. Radial Pressure Distributions over a 9-deg Half-Angle Spherically Blunted Cone at $M_\infty \sim 18$ and $\alpha = 10 \text{ deg}$	36
8. Radial Pressure Distributions over a 9-deg Half-Angle Spherically Blunted Cone at $M_\infty \sim 18$ and at Angle of Attack	38

<u>Figure</u>	<u>Page</u>
9. Radial Cross Sections of Shock and Constant Entropy Surfaces at Selected Stations (Z_B) versus Radial Angle (θ_B)	40
10. Streamline Patterns for a 9-deg Half-Angle Cone at $\alpha = 10$ deg from the GASL Body-Fixed Axis Solution. . . .	41
11. Pressure Contours for a 9-deg Half-Angle Cone at $\alpha = 10$ deg from the GASL Body-Fixed Axis Solution. . . .	43
12. Force and Moment Coefficients for Spherically Blunted Cones at $M_\infty \sim 18$	45
13. Variation of Normal-Force and Pitching-Moment Coefficient Slopes with Angle of Attack for a 9-deg Half-Angle Spherically Blunted Cone at $M_\infty \sim 18$	47

TABLES

I. Pressure Data from AEDC-VKF Tunnels	49
II. Test Conditions for AEDC-VKF Pressure Distribution Data	50
III. Modified Pressure Data from CAL 48-in. Shock Tunnel (Ref. 8)	51
IV. Test Conditions for CAL Pressure Distribution Data (Ref.8)	52
V. Experimental Force Coefficients and Free-Stream Conditions.	53
VI. Computed Force and Moment Coefficients ($\gamma = 1.4$) . . .	54

NOMENCLATURE*

A	Surface area / R_n^2
A_b	Base area, $\pi (R_b R_n)^2$
C_A	Axial-force coefficient, axial force / $q_\infty A_b$
C_D	Drag coefficient, $D / q_\infty A_b$

*Unless otherwise noted, all lengths are nondimensionalized with respect to the nose (sphere) radius.

C_{D_n}	Nose drag coefficient (0.964 for a sphere-cone)
C_F	General force coefficient representing the total force acting on vehicle, total force/ $q_\infty A_b$
C_L	Lift coefficient, $L/q_\infty A_b$
\vec{C}_{M_o}	Resultant-moment coefficient vector obtained by summing moments of all forces about point "O", moment/ $q_\infty A_b D_b R_n$
C_m	Pitching-moment coefficient, magnitude of Y-component of resultant-moment coefficient vector
C_{m_α}	Pitching-moment coefficient slope, $\partial C_m / \partial \alpha$, deg^{-1}
C_N	Normal-force coefficient, normal force/ $q_\infty A_b$
C_{N_α}	Normal-force coefficient slope, $\partial C_N / \partial \alpha$, deg^{-1}
C_p	Pressure coefficient, $(p - p_\infty)/q_\infty$
C_∞	Chapman-Rubesin viscosity coefficient, $(\mu_w / \mu_\infty) (T_\infty / T_w)$
D	Drag force along the free-stream velocity vector
D_b	Vehicle base diameter
d	Vehicle nose (sphere) diameter
H_o	Stagnation enthalpy, ft^2/sec^2
L	Lift force normal to free-stream velocity vector
l	Body length, in.
M	Mach number
N	Force normal to body axis of symmetry
\vec{n}	Unit inward normal vector to surface
p	Pressure
p_o	Free-stream stagnation pressure, lb/in^2
p'_o	Normal-shock pitot pressure, lb/in^2
q_∞	Free-stream dynamic pressure, $\gamma_\infty p_\infty M_\infty^2 / 2$, lb/in^2
R_B	Body radius in body-fixed axis system
R_b	Vehicle base radius
$Re_\infty, \text{in.}$	Free-stream unit Reynolds number, in.^{-1}
Re_∞, l	Free-stream Reynolds number based on body length
R_n	Vehicle nose (sphere) radius, ft
\vec{r}	Radius vector from point "O" to body point

S/R	Entropy, dimensionless
s	Surface distance from the geometric nose of the model
T	Temperature, °K
U_{∞}	Free-stream velocity, ft/sec
\bar{v}_{∞}	Viscous parameter, $M_{\infty} \sqrt{C_{\infty}} / \sqrt{Re_{\infty,z}}$
X	Coordinate axis normal to Z positive downward
Y	Right-hand coordinate axis normal to x-z plane
Z	Coordinate axis along the free-stream velocity vector (wind-fixed axis) or along the axis of symmetry (body-fixed axis)
Z_c	Cheng's axial distance parameter, $[(Z_B + 1)/2] \sigma_c^2 / \sqrt{\epsilon C_{D_n}}$
Z_{cp}	Center of pressure location
α	Angle of attack, deg
γ	Ratio of specific heats (1.40 used herein)
ϵ	$(\gamma - 1)/(\gamma + 1)$
η	Angle defined by $\cos \eta = \vec{V} \cdot \vec{n} / \vec{V} $
θ	Polar angle measured in plane perpendicular to axis of symmetry from most windward streamline
σ_c	Cone half-angle, deg

SUBSCRIPTS

1, 2, 3	Denoted values of parameters at limits of integration for each region, at special values of Z and θ , or values of force coefficients for each like numbered region
B	Body axes
b	Base
i	Initial value in streamline program
n	Nose, or normal direction
o	Stagnation conditions
w	Wind axes, or wall
X_i, Z_i	$i = B, w$, that component of force in region acting in X_i or Z_i direction
∞	Undisturbed free-stream conditions

SECTION I INTRODUCTION

One function of experimental research is to test the applicability and range of validity of theoretical models. In fluid mechanics, as the velocity increases many problems appear such as compressibility, interactions of inviscid and viscous flow fields, and so-called "real gas" effects. On the one hand, the problem is often complicated by the inadequacy of the experimental results to clearly indicate the relative magnitudes of separate but coupled effects. On the other hand, theoretical models usually are only applicable to simple geometric and fluid mechanical models. Even with the aid of large digital computers, "exact" solutions are not possible for many problems of current interest in gas dynamics.

In recent years considerable attention has been given to the comparisons of ideal gas and perfect dissociating and ionizing gas characteristics solutions for sphere-cones at zero angle of attack, but similar comparisons have not been possible at angles of attack because of the lack of adequate theoretical models for analysis of the three-dimensional flow fields. The three-dimensional characteristics theory used in the present study was developed at the General Applied Sciences Laboratory (GASL) by Moretti et al. (Ref. 1). The only known published results from this theory for axisymmetric bodies are calculations done by Jenkins (Ref. 2) for spherically blunted cones at 0- and 5-deg angles of attack over the range of altitudes from 100,000 to 260,000 ft, Mach numbers from 9 to 30, and cone half-angles of 10 and 12 deg.

The present report presents comparisons between an ideal gas, inviscid, three-dimensional characteristic solution and experimental data for surface pressure distributions, forces and moments of a 0.3 nose-to-base radius ratio, 9-deg half-angle spherically blunted cone at $M_\infty = 18$ over a range of angles of attack from 0 to 20 deg. The experimental data were taken in a Reynolds number range where strong viscous effects on zero-lift drag were previously found by Whitfield and Griffith (Ref. 3). These experimental data at angle of attack will, however, be used to assess the limitations and validity of the characteristics solution.

Since the wind tunnel experimental data were taken in nitrogen, it was necessary to base the calculations on ideal gas ($\gamma = 1.4$) properties rather than the equilibrium air data available in the machine program. Previously published zero-lift experimental data taken in the AEDC, von Kármán Gas Dynamics Facility (VKF), hotshot tunnels by Whitfield and Griffith (Ref. 3), Griffith and Lewis (Ref. 4), and Lewis and Whitfield

(Ref. 5) were found to be in reasonably good agreement with their ideal gas analyses.

Most of the calculations to be presented herein were made using the GASL wind-fixed axis program (Ref. 1). However, during the latter stages of the calculations a new version of the program was published by GASL (Ref. 6) and was used for some of the calculations presented. The new program, denoted herein as the body-fixed axis program, is a modification of the wind-fixed axis program for axisymmetric bodies such that the calculation is done in body-fixed rather than wind-fixed axes. This procedure simplifies the analysis and somewhat improves the accuracy of the calculation. However, a comparison will be shown at one angle of attack which indicates that the differences are small, and thus the large body of calculations at all angles of attack was not recomputed using the new program. Included in the new program is a procedure for tracing the streamline patterns on the surface and within the inviscid shock layer. This program is important for many applications and was used in the present study to determine streamline patterns on the body and on one constant entropy surface within the shock layer.

Calculations were made at $\alpha = 5, 10,$ and 20 deg for comparisons with experimental data from the AEDC-VKF 50-in. and 100-in. hypervelocity tunnels (Gas Dynamic Wind Tunnels, Hypersonic (H) and (F)) and the 48-in. shock tunnel of the Cornell Aeronautical Laboratory (CAL). A machine program was developed by the first author and M. R. Reed which transformed the wind-fixed axis solution for the body surface pressure distribution to the corresponding body-fixed axis and interpolated the resulting pressure distribution for comparison with the experimental data. An additional machine program was written to integrate the resulting pressure distribution and compute the normal-force coefficient, C_N , and pitching-moment coefficient, C_m , for comparison with available experimental data. Also, for comparison with the numerical results based on the GASL program and experimental data, the results of the modified Newtonian theory are presented. In addition to the above comparisons, normal-force and pitching-moment slopes, C_{N_α} and C_{m_α} , were computed and are compared with numerical differentiation of the experimental data.

SECTION II INVESTIGATION

2.1 THEORETICAL CONSIDERATIONS

The numerical analysis presented herein used the GASL wind-fixed axis program to obtain the body surface pressure distribution for a range

of angles of attack. The wind-fixed axis solution was then transformed to body-fixed axis and interpolated for integration and comparison with the experimental data. A brief discussion of the GASL program is presented below.

The initial supersonic data were obtained from an inverse blunt body solution for a unit sphere at $M_\infty = 18$ in an ideal gas at one atmosphere pressure. The resulting blunt body flow field solution was interpolated along a surface normal to the wind-fixed axis. The GASL program uses the method of characteristics in three dimensions to compute from these initial data the fluid properties in the inviscid supersonic flow field about spherically capped lifting bodies. The technique is such that computations are made in two mutually perpendicular planes using the intersections of the characteristic surfaces in the flow field with these planes as characteristic lines. The intersection of the characteristic lines represents a solution point which is common to both planes. For the present calculations, a cylindrical coordinate system was used with Z_w measured from the center of the sphere in the wind direction, the radius R , normal to the Z_w axis, and the polar angle, θ_w , measured from the most windward streamline. For the GASL calculations presented, the shock layer was defined by eleven positions between the body and the shock and 10-deg increments in θ_w . The calculations were made along the Z_w axis such that the solutions were obtained for each θ_w between 0 and 180 deg in the Z_w plane, and then a subsequent Z_w plane was selected and the procedure was repeated.

Inasmuch as the solutions were obtained in Z_w planes with θ_w measured about the Z_w axis, it was necessary to shift the Z_w axis periodically as the calculation proceeded along the body. Whenever the Z_w axis deviated by more than a fixed amount from the axis of symmetry of the body, a "change-of-frame" was made. Figure 1 shows a sketch of the cone nomenclature and coordinate system. The criteria for determining how often a change-of-frame was necessary are arbitrary, and the results of different scheduled changes-of-frame are reported herein.

The transformation of the GASL wind-fixed axis pressure distribution was made using the appropriate equations for a selected body point from which the equivalent Z_w and θ_w were determined. The GASL results were then interpolated by a four-point Lagrangian interpolation formula to obtain the pressure at desired points. The resulting interpolated pressure distribution was integrated by the trapezoidal rule to obtain the forces and moments. Also for comparison, the modified Newtonian theory was used to calculate a pressure distribution and then integrated to obtain the forces and moments.

A detailed discussion of the pertinent equations and techniques used in the present analysis is given in the Appendix.

The GASL body-fixed axis three-dimensional characteristics solution (Ref. 6) was essentially that described above except that the calculation was done in body-fixed rather than wind-fixed axes. The initial data were, however, obtained by rotating the wind-fixed axis sphere solution to obtain the initial data in a plane perpendicular to the body axis of symmetry.

2.2 EXPERIMENTAL STUDIES

The experimental data presented herein were obtained in two AEDC-VKF hotshot tunnels, Tunnels H and F, and the 48-in. reflected shock tunnel of the Cornell Aeronautical Laboratory (CAL). The AEDC-VKF and CAL tests were conducted in nitrogen and air, respectively. All data were taken on a 0.3 nose-to-base radius ratio 9-deg half-angle spherically blunted cone over an angle-of-attack range of 0 to 20 deg. A comparison of some of the experimental data presented herein from the VKF and CAL facilities was previously presented by Edenfield in Ref. 7, and the reader is referred to that report for a detailed description of the experimental programs. However, tables are presented herein which list all the experimental data used in the present study. Table I gives the pressure distribution data from the VKF tunnels, referenced to the measured test section pitot pressure. Each column gives a gage location on the model, and the coordinates of each orifice are noted. The axial distance is referenced to the nose radius and measured from the center of the spherical cap, whereas the surface distance is measured from the nose of the model. The model radial angle, θ_B , was measured from the most windward streamline direction. The test conditions associated with the data presented in Table I are given in Table II.

The data for the CAL investigation were obtained from Ref. 8. The pressure data are presented in Table III in a modified form, and the tunnel test conditions are given in Table IV. The data given in Ref. 8 were referenced to a computed p'_0 based on previous tunnel calibrations. These data were modified so that at zero angle of attack the measured stagnation point pressure was used as the reference, and at angles of attack the pressure measured nearest the stagnation point was corrected to the stagnation point by modified Newtonian theory. The latter value is denoted herein as p'_0^* .

Finally, tabulations of all the force and moment coefficients are presented in Tables V and VI. The experimentally determined coefficients

and the associated tunnel test conditions are given in Table V, and the computed coefficients are given from the GASL and modified Newtonian numerical solutions in Table VI.

SECTION III RESULTS AND DISCUSSION

3.1 ZERO-LIFT PRESSURE DISTRIBUTIONS

An obvious test of any three-dimensional flow field solution is comparison with a two-dimensional or axisymmetric solution where both theories are applicable, viz., at zero angle of attack. Such a comparison is shown in Fig. 2 between the GASL solution and the results from an AEDC axisymmetric ideal gas characteristics program developed by ARO, Inc. The comparison is made in terms of $C_p/2\sigma_c^2$ against $Z_c = [(Z_B + 1)/2] \sigma_c^2 / \sqrt{\epsilon C_{D_n}}$. The correlation parameter, Z_c , was proposed by Cheng (Ref. 9), and Griffith and Lewis (Ref. 4) modified Cheng's correlation parameter, $p/M_\infty^2 p_\infty \gamma \sigma_c^2$, to read $C_p/2\sigma_c^2$ in order to account for the fact that the condition imposed by Cheng, $p \gg p_\infty$, frequently is not satisfied. An improved correlation with experimental data was obtained in this manner.

Some experimental data from AEDC-VKF and CAL are also shown in Fig. 2. Of primary interest here is the comparison between the AEDC ideal gas axisymmetric solution and the GASL wind-fixed axis solution. The differences are believed to be in the computation techniques used and the numerical accuracy of each solution. As noted earlier, the GASL program obtains a solution at each point represented by the intersection of two characteristic lines in a θ_w plane. This point also lies in a Z_w plane, and the points between the body and the shock in each plane are interpolated at eleven points in the R direction and eighteen points in the θ direction. At angles of attack, large variations in the slopes of the characteristics lines occur from the windward to the leeward side of the body, and this implies large deviations in their intersections from a single Z_w plane. This requires the convergence criteria to be relatively loose at angle of attack, and thus the accuracy of the numerical solution suffers at zero angle of attack. However, when the convergence criteria in the AEDC axisymmetric program are not met, the mesh size is reduced by doubling the number of points along a right running characteristic from the shock to the body. This latter procedure generates a finer network of points, and the solution is inherently more accurate. Therefore, the difference between the AEDC and GASL wind-fixed axis solution at zero angle of attack must be viewed as an indication of the built-in inaccuracy within the GASL method.

The differences between the experimental data and the AEDC axisymmetric characteristics solution shown in Fig. 2 have recently been investigated by Lewis and Whitfield (Ref. 5). The results of that study showed that the difference can be accounted for on the basis of a combined inviscid-viscous interaction solution. They showed that for the range of conditions of interest in the present study, the correlation of $C_p/2\sigma_c^2$ against Z_c as given previously by Griffith and Lewis (Ref. 4) was in good agreement with the results of the inviscid-viscous interaction solution. Therefore, at zero angle of attack the differences between the experimental data and the AEDC inviscid characteristics solution are believed to be primarily caused by viscous effects, and the differences between the two inviscid solutions are believed to be numerical.

When considering the angle-of-attack results, one should keep in mind these comments which only strictly apply at zero angle of attack. The effects of numerical accuracy and viscous interaction will remain important at angles of attack and particularly at small angles of attack. Effects of viscous interaction, at least on the windward side, will be reduced with increasing angle of attack.

3.2 SURFACE PRESSURE DISTRIBUTIONS AT ANGLES OF ATTACK

3.2.1 Effects of Change-of-Frame

In performing the calculations with the GASL wind-fixed axis program at angles of attack, it was necessary to select positions along the body at which changes-of-frame of reference were made. Such changes-of-frame were made by specifying the Z_w at which the change was to occur and the incremental change in X_w . Since both quantities were arbitrarily chosen, it was of interest to see the effects of these quantities on the solution. To investigate these effects several computer solutions were obtained for the 10-deg angle-of-attack case with a wide variation in the change-of-frame schedules. The results of these comparisons will now be presented.

Three different solutions were obtained at an angle of attack of 10 deg with three change-of-frame schedules. Figure 3 is a sketch of the model showing the changes-of-frame for the three solutions denoted solutions 1, 2, and 3. Solutions 1 and 2 differ only after the fourth change-of-frame, and solution number 3 was selected such that $\Delta X_w = 0.2$; that is, whenever $\Delta Z_w \tan \alpha = 0.2$ a change-of-frame was made. All three solutions were found to be practically identical to change-of-frame number 5 for solution number 2 and to change-of-frame number 10 for solution number 3. However, solution number 1 departed radically from

solutions number 2 and 3 further downstream. Figure 3b shows the radial surface pressure distribution for the three solutions at two Z_B stations where experimental data were available for comparison. The comparison shows solution number 2 is considerably improved over solution number 1. It is interesting to note, however, that a further increase in the number of changes-of-frame had no significant effect on the distribution as shown by solution number 3. Since the criteria for making a change-of-frame are arbitrary, it does appear that one should investigate the effects by making comparisons of the type shown above.

The solution from the GASL body-fixed axis program is also shown in Fig. 3b. Comparison of the body-fixed axis solution and solution number 3 shows excellent agreement except near the most windward and most leeward streamlines. There are also some small differences in the region of minimum pressure. It is also of interest to note that the experimental pressure distributions along the most windward ($\theta_B = 0$) and most leeward ($\theta_B = \pi$) streamlines are in better agreement with the body-fixed axis solution. Because of this and certain overall improvements in smoothness of the solution, the body-fixed axis solution is preferred. However, as noted above, most of the calculations for this study were completed before the body-fixed axis program became available.

Solutions were obtained for $\alpha = 5, 10$, and 20 deg with change-of-frame schedules similar to those of solution number 1 shown in Fig. 3a. Only after examination of solution number 1 and the "wells" of low pressure noted were the two other solutions obtained for $\alpha = 10$ deg. The $\alpha = 5$ -deg case did not exhibit the formation of any low pressure wells. However, for $\alpha = 20$ deg the problem of low pressure wells became more acute, and the solution failed to converge on the leeward side at a Z_w station only about one-third of the total length of the body. In order to continue the solution over the remainder of the body, it was necessary to delete θ_w planes in the leeward region downstream of the Z_w plane where the failure occurred. This was accomplished by limiting the maximum value of θ_w to less than the value where the failure occurred. Before the $\alpha = 20$ -deg solution was continued an $\alpha = 15$ -deg solution was obtained with a change-of-frame criteria similar to that in solution 3 above, viz. $\Delta Z_w \tan \alpha = 0.2$. Difficulties similar to those encountered in the $\alpha = 20$ -deg solution were observed for the $\alpha = 15$ -deg case. Except in the latter case, the failure occurred about two-thirds of $Z_{B_{max}}$. However, it was necessary again to delete θ_w planes to continue the solution. Because of this result, it was felt that increasing the changes-of-frame in the 20 -deg case would not improve the solution significantly, since deleting θ_w planes in the leeward region is tantamount to removing the leeward boundary condition

from the solution, viz., the requirement that the cross velocity be zero along the most leeward streamline. Little can be said regarding the validity of solutions obtained under conditions where θ_w planes are deleted. Therefore, only representative radial distributions will be presented to illustrate the character of the solutions upstream and downstream of the Z_w plane where the solutions failed to converge. Figure 4 shows the change-of-frame schedules for all angles of attack used in the wind-fixed axis solutions.

3.2.2 Windward and Leeward Streamline Pressure Distributions

The computed longitudinal pressure distributions on the windward ($\theta_B = 0$) and leeward ($\theta_B = \pi$) streamlines on the conical portion of the body are compared with experimental data in Figs. 5a, b, and c for $\alpha = 5, 10$, and 20 deg. Lack of experimental data at $\alpha = 15$ deg prevented a similar comparison for that case. The experimental data show considerable scatter, but in comparison with the computed distributions, the agreement is reasonably good. The agreement is improved with increasing angle of attack, especially along the most windward streamline, and as noted above, viscous effects are reduced with increasing angle of attack. At $\alpha = 10$ deg the distributions along the most windward and leeward streamlines from the body-fixed solution are also shown, and the results are seen to be in better agreement than the corresponding wind-fixed axis solutions.

At $\alpha = 5$ and 10 deg along the leeward streamlines the agreement between the experimental and numerical pressure distributions is not as good as for the windward streamlines. The agreement improves somewhat with angle of attack. However, because of the low pressure region, experimentally there will be a thick laminar boundary layer interacting with the inviscid outer flow. This viscous interaction will induce a pressure increment as noted previously for zero angle of attack. Since the solution along the leeward streamline at 20 -deg angle of attack only existed over approximately the first one-third of the body, the comparison shown in Fig. 5c is interesting, but conclusive statements regarding the results are not possible.

It is well known that the nose-dominated region of spherically blunted slender cones extends many nose diameters downstream. That is, for a cone of small half-angle (e. g. $\sigma_c \leq 9$ deg), the inviscid blunt cone surface pressure distribution will require more than 60 nose radii before approaching the inviscid sharp cone value. As the cone angle increases the nose-dominated region is reduced in extent. The pressure distribution is characterized by a strong overexpansion and recompression to the sharp cone value. It is of interest to note at zero-lift that

the cone under investigation ends at approximately the minimum in the overexpansion and recompression region. It is also of interest to note from Figs. 5a and b that the same effects of the nose-dominated region are observed along the windward streamlines at $\alpha = 5$ and 10 deg.

Axisymmetric characteristic solutions were obtained for spherically blunted cones with half-angles $\sigma_c = 9 + \alpha$ deg. Figure 5d shows a comparison of the axisymmetric solutions for $\sigma_c = 14$ and 19 deg and the "corresponding" GASL solutions for $\alpha = 5$ and 10 deg. Of primary interest here is the approximately constant difference between the solutions for the range of Z_w shown and the smaller difference between solutions as σ_c or α increases. This is in agreement with the results and comments given for $\alpha = 0$. It is also of interest to note the small effects of cross flow along the most windward streamline as indicated by the good agreement between the axisymmetric and three-dimensional solutions. It thus appears that an axisymmetric characteristics solution adequately predicts the most windward streamline pressure level and the overexpansion and recompression regions for an equivalent angle, $\sigma_{c_{equiv}} = \sigma_c + \alpha$. Except in the asymptotic limit of large Z_B or large cone angle, σ_c , modified Newtonian is unable to predict the correct pressure level and, in any event, is unable to predict the overexpansion and recompression pressure region. The axisymmetric calculations gave $p/p_0 = 0.0594, 0.1230, \text{ and } 0.2440$ for $\alpha = 5, 10, \text{ and } 20$ deg, respectively, for the limiting surface pressure ratio, and modified Newtonian theory gave corresponding values of $0.057, 0.105, \text{ and } 0.236$. A comparison with the experimental data of Table I shows good agreement with these values. The limits of applicability of the Newtonian theory will be clearer from comparisons of predicted and experimental radial pressure distributions at angles of attack.

3.2.3 Radial Pressure Distributions

Comparisons of the radial pressure distributions at several positions along the body computed by the GASL wind-fixed axis program and modified Newtonian are presented in Fig. 6 for $\alpha = 5$ deg. The available experimental data are also shown for comparison. Only at $Z_B = 10.675$ were data available for a range of the viscous hypersonic parameter, \bar{v}_∞ . The trends of the distributions from the GASL wind-fixed axis solution and experiment are in good agreement. As noted before, the experimental data are strongly viscous affected especially at this low angle of attack. It should be noted here that the CAL experimental data are for $M_\infty = 13$, whereas the calculation was made for $M_\infty = 18$. It would be surprising indeed if the differences shown were strongly Mach number dependent. Moreover, the Reynolds numbers for the experiments were sufficiently high ($\bar{v}_\infty = 0.031$) that it would be equally surprising if the

differences between experiment and numerical results were attributable entirely to viscous interaction. Thus, further calculations and experiments at the CAL conditions would be of interest at $\alpha = 5 \text{ deg}$.

Modified Newtonian theory is also shown in Fig. 6 for comparison with the GASL solution and experimental data. The comparison shows reasonably good agreement over the windward side and far downstream of the nose. It is under these conditions, of course, where the shock wave is nearly parallel to the body that one would expect Newtonian theory to better apply; however, even over the windward side the GASL solution better predicts the trends of the experimental data.

Radial distributions for $\alpha = 10 \text{ deg}$ are shown in Fig. 7 for comparison with the considerably larger body of experimental data. It was, in fact, this body of data which influenced the decision to obtain the GASL body-fixed axis solution for this condition. In contrast to the $\alpha = 5\text{-deg}$ experimental data, the experimental scatter here appears to be considerably reduced, and the agreement with the numerical surface pressure distribution is quite good to $\theta_B = 120 \text{ deg}$. The largest body of experimental data exists for this case at $Z_B = 10.675$, and as in the $\alpha = 5\text{-deg}$ case, there was no consistent trend of the experimental data with Reynolds number. Modified Newtonian theory is seen to be in better agreement with the experimental data in the windward region than in the previous $\alpha = 5 \text{ deg}$ case. This is not surprising since the shock wave lies closer to the body along the windward side and is more nearly parallel with the body. Modified Newtonian theory also again fails in the leeward region, and comparisons of the GASL solution and experimental data also show poor agreement on the leeward side of the body.

The discovery of the inviscid low pressure "wells" on the leeward side of the body at $\alpha \geq 10 \text{ deg}$ and their apparent strong effects on the solution was one of the more interesting aspects of the present study. These low pressure regions have been observed experimentally on other axisymmetric bodies at low Mach numbers and high Reynolds numbers. However, the experimental data at $M_\infty \sim 18$ did not indicate their existence. A well was first noted in the distributions shown here at $Z_B = 5.250$. However, it was found that once the well began to develop the minimum pressure tended to drop rather rapidly with increasing Z_B and ultimately led to the failure of the solution to converge. The $\alpha = 10\text{-deg}$ calculation was continued, and the solution failed to converge at $Z_b \approx 22$. The experimental data do not appear to support the development of the low pressure wells. However, viscous effects could mask the effect and almost certainly would strongly affect the pressure distribution in this region.

There appear to be two simple explanations for the development of the inviscid wells. First, consider the flow along a streamline on the

body surface. The fluid expands along the streamline from the high pressure windward side. However, as the leeward side of the body is approached it is necessary for the streamlines to be turned back toward the free-stream direction since the streamlines cannot cross. This bunching of streamlines near the most leeward streamline* will create a ridge of high pressure. The second explanation is related to the alleged loose convergent criterion discussed earlier. At the higher angles of attack the right running characteristics on the leeward side of the body are more nearly parallel with the body so that the distance between the intersections becomes large. Therefore, the possibility of errors affecting the solution is increased. The first explanation appears physically reasonable. However, in any numerical solution as complex as this the effects of numerical inaccuracies can never be entirely neglected. In any event, let it suffice to say that a problem area exists in the simple, straightforward application of the numerical results.

Finally, distributions for $\alpha = 15$ and 20 deg are shown in Figs. 8a and b, respectively, to further illustrate the development of the low pressure wells and to show the distributions at $Z_B = 10.675$ obtained downstream of the leeward region cut-off plane. Notice the excellent agreement between the GASL solution and modified Newtonian theory. However, in view of the procedure used to obtain the GASL solution (viz. deleting θ_w planes) the results must be viewed with caution.

Beyond the interest in the comparisons with experimental pressure distributions shown here, the results should be useful in conjunction with a three-dimensional boundary-layer analysis. Examination of the surface pressure distributions for $\alpha = 10$ deg leads one to consider the effects of the low pressure wells and strong adverse pressure gradients on a boundary-layer solution. It is well known that laminar boundary layers cannot sustain strong adverse pressure gradients, and the adverse gradient shown for $\alpha = 10$ deg and $Z_B = 12.55$ in Fig. 7 would be sufficient to separate a laminar boundary layer. To further investigate this problem, the following hypothetical case was studied.

3.3 PRESSURE AND STREAMLINE DISTRIBUTIONS ON A CONSTANT ENTROPY SURFACE

To investigate the behavior of the pressure distribution within the shock layer, a constant entropy surface ($S/R = 15.754$) was considered at $\alpha = 10$ deg. The entropy at the intersection of the initial surface and the bow shock wave at $\theta_B = 0$ was chosen. The initial surface was a plane

*The authors are indebted to E. A. Sanlorenzo, General Applied Sciences Laboratory, for an interesting discussion of this point.

normal to the body axis at $Z_B = -0.33787$ and intersected the bow shock wave and $\theta_B = 0$ at 60.25 deg (acute angle measured at the center of the sphere from Z_w axis). This value of the entropy is the minimum for the complete three-dimensional characteristics flow field solution and is independent of angle of attack for these initial surface data. It should be emphasized that this constant entropy surface (bounding an "entropy layer") is not the "edge" of the boundary layer but is rather a surface within the inviscid shock layer along which certain data were obtained.

The GASL streamline tracing program was used to interpolate the inviscid shock layer, establish the coordinates of the constant entropy surface, trace the streamlines on that surface, and interpolate for the flow field variables along the streamlines. Figure 9 shows the cross sections of the body, shock wave, and constant entropy surface at selected stations for $\alpha = 10$ deg. Figure 10 shows the streamline distributions on the body and on the constant entropy surface. Note the significantly reduced curvature of the streamlines on the constant entropy surface relative to those on the body surface. More significant comparisons are shown, however, in Fig. 11 where pressure contours on the body surface and the constant entropy surface are shown. The development of the low pressure wells on the body surface is easily seen in Fig. 11a, and a low pressure well is seen to form at $Z_B \approx 18$ on the constant entropy surface. Note, however, that the wells begin to form on the constant entropy surface approximately three times further downstream than on the body surface. It should also be mentioned here that the solution failed to converge at $Z_B \approx 22$ on the body surface. Thus, the formation of the well and the associated adverse pressure gradient on the constant entropy surface would indicate that a much smaller adverse pressure gradient exists within the shock layer than on the body surface. These results, although only qualitative, are believed to be significant for they clearly show that whereas a boundary-layer solution would separate based on the inviscid wall pressure distribution, a similar calculation based on the boundary-layer-edge pressure distribution (simulated here by the constant entropy surface) would be less subject to strong adverse pressure gradients.

Comparisons between the experimental surface pressures and the computed pressures on the constant entropy surface at $\alpha = 10$ deg are shown in Fig. 7. The agreement between experiment and the constant entropy surface data is better than a similar comparison with the pressure distribution along the inviscid wall. Because of the arbitrariness of the constant entropy surface, only the trends should be considered here, and those trends are in good agreement with the experimental data.

3.4 FORCE AND MOMENT COEFFICIENTS

The second area of primary interest in the present report is a comparison between calculated and experimentally measured force and moment coefficients. Numerical results will be presented based on surface pressure distributions obtained from the GASL solutions and modified Newtonian theory. In addition, numerical and experimental normal-force and pitching-moment coefficients will be used to calculate the slopes, C_{N_α} and C_{m_α} . However, before discussing the results at angle of attack a few comments will be made on previous studies at zero-lift.

3.4.1 Zero-Lift Drag Studies

The effects of viscous interaction on wall measurable quantities have received much attention in VKF in recent years. The primary shape considered in those studies was also a 0.3 bluntness 9-deg half-angle cone. The effects of viscous interaction on zero-lift drag were studied by Whitfield and Griffith (Refs. 3 and 10). More recently, Lewis and Whitfield (Ref. 5) re-examined the experimental data and earlier analysis at zero-lift. Two important results from these studies should be noted here: First, for the range of experimental conditions of the present study the total viscous drag was approximately twice the inviscid pressure drag. Secondly, the application of the most exact currently available theories (viz. characteristics and nonsimilar boundary-layer solutions) at zero-lift underestimated the total drag, thus implying significant contributions by other so-called "second-order" boundary-layer effects (especially shock generated external vorticity, cf. Ref. 5).

3.4.2 Angle-of-Attack Results

Figure 12 shows a comparison of experimental and theoretically predicted force and moment coefficients for a 9-deg half-angle spherically blunted cone over a range of angles of attack, $\alpha = 0$ to 20 deg. The experimental data shown from AEDC-VKF and CAL were all chosen at nominal values of $\bar{v}_\infty = 0.05$ and wall-to-stagnation temperature ratio $T_w/T_0 = 0.1$. The present results (in agreement with the previous results of Whitfield and Wolny (Ref. 11)) show that the inviscid normal-force and pitching-moment coefficients, C_N and C_m , are in reasonably good agreement with the experimental data over the entire angle-of-attack range. However, in agreement with the zero-lift data, the axial-force coefficient, C_A , is strongly viscous affected over the angle-of-attack range considered herein. The trends of the numerical and experimental results are, however, in reasonably good agreement. For comparison, Harris' results from the NASA helium tunnel (Ref. 12) and a $R_n/R_b = 0.255$

10-deg half-angle cone at $M_\infty = 19$ and $Re_\infty/in. = 200,000$ (corresponding to a $\bar{v}_\infty = 0.016$) are also shown. The agreement between the present analysis for $\gamma = 7/5$ and the experimental data in helium ($\gamma = 5/3$) is excellent for $\alpha \leq 7.5$ deg.* At a Reynolds number almost one order of magnitude higher than the AEDC-VKF and CAL experimental data, the viscous-induced drag should, of course, be substantially reduced. The strong effects of viscous interaction on the axial-force coefficient are also shown on Fig. 12d with a plot of lift-to-drag ratio against angle of attack. From this figure it can be seen that the integrated GASL results substantially overpredict the lift-to-drag ratio because of the rather large viscous-induced axial-force increment. Again, it is also interesting to note that the NASA helium tunnel data are in substantial agreement with the integrated GASL results.

Modified Newtonian theory was also used to compute the force and moment coefficients for the range of angles of attack, $\alpha \leq 20$ deg, Fig. 12. Based on the comparison with the experimental data, the theory is not clearly inferior to the GASL prediction and appears to be a reasonably good approximation for the normal-force and pitching-moment coefficients, C_N and C_m . Moreover, only relatively small differences exist between theoretical predictions of C_A based on modified Newtonian theory and the integrated GASL results. The area of largest difference between the two theories occurs at the lower angles of attack ($\alpha < 10$ deg). The significant differences between the predicted values of the normal-force coefficient, C_N , are reflected in the lift-to-drag ratio curve, where again it should be noted that better agreement exists between the integrated GASL results and the experimental data than was found using the modified Newtonian theory.

3.4.3 Stability Derivatives

Stability analyses make use of normal-force and pitching-moment coefficient slopes, C_{N_α} and C_{m_α} . It was, therefore, of interest to examine the integrated GASL and modified Newtonian results for predictions of those slopes. The coefficients C_N and C_m are again shown in Fig. 13 based on the two theoretical models. In addition, the variation of C_{N_α} and C_{m_α} with angle of attack is also shown. An experimental uncertainty of ± 10 percent was associated with the experimental AEDC-VKF and CAL data and is also shown. The minimum and maximum of the experimental

*The differences in cone geometry, Mach number, and γ make a quantitative comparison between the numerical results at $\gamma = 1.4$ and the helium tunnel experimental data impossible; the trends of the experimental data are as expected.

data, treated as two separate curves, were interpolated at 2.5-deg intervals with a four-point Lagrangian interpolation formula over the range $\alpha = 0$ to 15 deg. The results were differentiated numerically with a cubic spline, and the resulting slopes are shown as shaded areas in the figure. Of most importance here is the trend of the results rather than the absolute values of the normal-force and pitching-moment slopes. Absolute differences between experiment and theory are difficult to determine because of the uncertainty in the experimental data and the errors induced by numerical differentiation. It is clear from the results shown that the integrated GASL results over the range $\alpha = 0$ to 10 deg give trends that are in good agreement with the experimental data, whereas the modified Newtonian theory results are in poor agreement with the experimental trends.

SECTION IV CONCLUDING REMARKS

Comparisons have been made between an ideal gas ($\gamma = 1.4$) three-dimensional characteristics solution (GASL), the modified Newtonian theory and available experimental data for pressure distributions, force and moment coefficients, and stability derivatives for a 9-deg spherically blunted cone over the angle-of-attack range from 0 to 20 deg. The results were as follows:

1. The effects of arbitrarily prescribed change-of-frame criteria in the wind-fixed axis solution were investigated. The criteria $\Delta Z_w \tan \alpha = 0.2$ gave good results over the range of angles of attack and axial distance considered in the present study. Some improvement was found by using the body-fixed axis solution and is to be preferred in further studies of axisymmetric bodies at angles of attack. However, the differences found in surface pressure distributions were small, and the wind-fixed axis results given in the present report were only slightly affected.
2. A comparison between the GASL results and an axisymmetric characteristic solution at zero angle of attack indicated differences in the pressure distribution along the body of about 10 percent. The GASL result was found to be uniformly below an AEDC ideal gas axisymmetric solution. Previous studies have shown that differences between inviscid solutions and experimental data of the order of 10 percent can be explained as the viscous-induced pressure increment. Therefore, caution should be exerted when using the GASL wind-fixed solution to predict pressure distribution at zero angle of attack.

3. Predictions of windward streamline pressure distributions from the GASL results were found to be in better agreement with the experimental data with increasing angle of attack, and at 10-deg angle of attack the comparison was quite good. Because of the necessity of dropping θ_w planes at $\alpha = 15$ and 20 deg, the comparison of windward streamline pressure distribution at $\alpha = 20$ deg was interesting, but conclusive statements regarding the comparison were not possible.
4. Comparison of experimental and theoretically predicted radial pressure distributions based on the GASL and modified Newtonian theories showed the GASL results to be uniformly superior in predicting the trends of the experimental data. At low angles of attack the differences between the GASL results and the experimental data are believed to be primarily caused by viscous effects. Since θ_w planes were deleted for $\alpha \geq 10$ deg, comparison of leeward side pressure distributions was not possible over much of the body at $\alpha = 20$ deg. Low pressure "wells" were found to develop along the surface at $\alpha \geq 10$ deg. The experimental data did not indicate such formations; however, further experimental data are needed along the leeward side at angles of attack.
5. The possible effects of the low pressure "wells" were investigated along a constant entropy surface within the inviscid shock layer. The curvature of the streamlines and the depth of the low pressure wells were substantially less along the constant entropy surface than along the body surface. The agreement between the experimental wall and the computed, constant entropy surface pressures was better than with the computed inviscid wall pressures.
6. Force and moment coefficients were approximated reasonably well by both the integrated GASL wind-fixed axis solution and those based on modified Newtonian theory. The normal-force and pitching-moment coefficients, C_N and C_m , were found to be in good agreement with the experimental data when computed from the GASL results. In agreement with previous studies of viscous effects on zero-lift drag, the predicted inviscid axial-force coefficient, C_A , was found to be about 40 percent below the experimental data at $M_\infty \sim 18$ over the entire angle-of-attack range. Strong viscous effects were reflected in the lift-to-drag ratio comparison where all theoretical results considerably overpredicted the lift-to-drag ratio.
7. Normal-force and pitching-moment coefficients, C_N and C_m , were numerically differentiated with respect to angle of attack, α .

Comparisons showed results based on the integrated GASL data were in better agreement with the trends of the experimental data than were the results based on modified Newtonian theory.

The results of the present study indicate the GASL characteristic solution should be a valuable tool when coupled with a three-dimensional boundary-layer theory for studying hypersonic viscous effects at angles of attack. Certain limitations and deficiencies were noted which deserve further study (such as the comparison of pressure distributions at zero angle of attack).

APPENDIX

FORCE AND MOMENT EQUATIONS

For comparison with the experimental (body-fixed) pressure distributions, it was convenient to machine interpolate the GASL wind-fixed axis solution. The resulting surface pressure distribution was integrated to obtain the force and moment coefficients for comparison with the experimental data. The transformation, derivation of the force and moment equations, and the details regarding the use of the modified Newtonian theory will be given below.

TRANSFORMATIONS

It can be seen from Fig. 1 that the two axes systems of interest are related by a rotation transformation, which in matrix form is as follows:

$$\begin{pmatrix} X_w \\ Y_w \\ Z_w \end{pmatrix} = \begin{pmatrix} \cos \alpha & 0 & \sin \alpha \\ 0 & 1 & 0 \\ -\sin \alpha & 0 & \cos \alpha \end{pmatrix} \begin{pmatrix} X_B \\ Y_B \\ Z_B \end{pmatrix} \quad (1)$$

In the body-axis system, the X and Y coordinates were replaced by the polar coordinates R_B and θ_B , so that

$$X_B = R_B \cos \theta_B, \quad Y_B = R_B \sin \theta_B \quad (2)$$

where X_B , Y_B , and R_B are nondimensionalized with respect to the nose radius. Using the results in Eq. (2) in the scalar form of Eq. (1) the result was obtained:

$$\left. \begin{aligned} X_w &= R_B \cos \theta_B \cos \alpha + Z_B \sin \alpha \\ Y_w &= Y_B = R_B \sin \theta_B \\ Z_w &= Z_B \cos \alpha - R_B \cos \theta_B \sin \alpha \end{aligned} \right\} \quad (3)$$

The geometry was such that

$$\theta_B = \tan^{-1} (Y_B/X_B), \quad \theta_w = \tan^{-1} (Y_w/X_w)$$

Thus,

$$\theta_w = \tan^{-1} [R_B \sin \theta_B / (R_B \cos \theta_B \cos \alpha + Z_B \sin \alpha)] \quad (4)$$

so that Eqs. (3) and (4) are the transformation equations from body-fixed to wind-fixed axes.

Inasmuch as the reference axis for θ_w within each change-of-frame was the shifted Z_w , there was a correction on X_w in computing $\tan \theta_w$.

This correction was to decrease X_w by the sum of the ΔX_w 's for all changes-of-frame up to the point considered. The result is

$$\theta_w = \tan^{-1} \left[R_B \sin \theta_B / (R_B \cos \theta_B \cos \alpha + Z_B \sin \alpha - \sum_{i=1}^m \Delta X_{w_i}) \right] \quad (5)$$

where m is the number of changes-of-frame to Z_w . For a given Z_B and θ_B , Eq. (5) and the last of Eq. (3) were used to determine Z_w and θ_w . The pressure was computed by the four-point Lagrangian formula,

$$Y = F_1(x) Y_1 + F_2(x) Y_2 + F_3(x) Y_3 + F_4(x) Y_4$$

where

$$F_1(x) = \frac{(x-x_2)(x-x_3)(x-x_4)}{(x_1-x_2)(x_1-x_3)(x_1-x_4)}, \quad F_2(x) = \frac{(x-x_1)(x-x_3)(x-x_4)}{(x_2-x_1)(x_2-x_3)(x_2-x_4)}$$

$$F_3(x) = \frac{(x-x_1)(x-x_2)(x-x_4)}{(x_3-x_1)(x_3-x_2)(x_3-x_4)}, \quad F_4(x) = \frac{(x-x_1)(x-x_2)(x-x_3)}{(x_4-x_1)(x_4-x_2)(x_4-x_3)}$$

and the subscript numbers represent the known values to be interpolated in both Z_w and θ_w . More specifically, for a given Z_B and θ_B the corresponding Z_w and θ_w were computed. The computer searched the GASL results for four sets of pressures which bracketed both Z_w and θ_w , preferably two on each side; however, as the end of the body or a change-of-frame was approached, a three and one or an end point interpolation was used. In all, five interpolations were necessary to define the pressure at a point--four were required to determine the pressure at each of the four known θ_w 's in the desired Z_w plane, and a final interpolation on θ_w gave the desired result. In the present analysis, these calculations were performed at 0.2 intervals in Z_B from -1 to 14.644 with additional special Z_B values for comparison purposes. In each Z_B plane, pressures were computed in 10-deg increments in θ_B . The resultant pressures were printed out and stored for later use in the force equations.

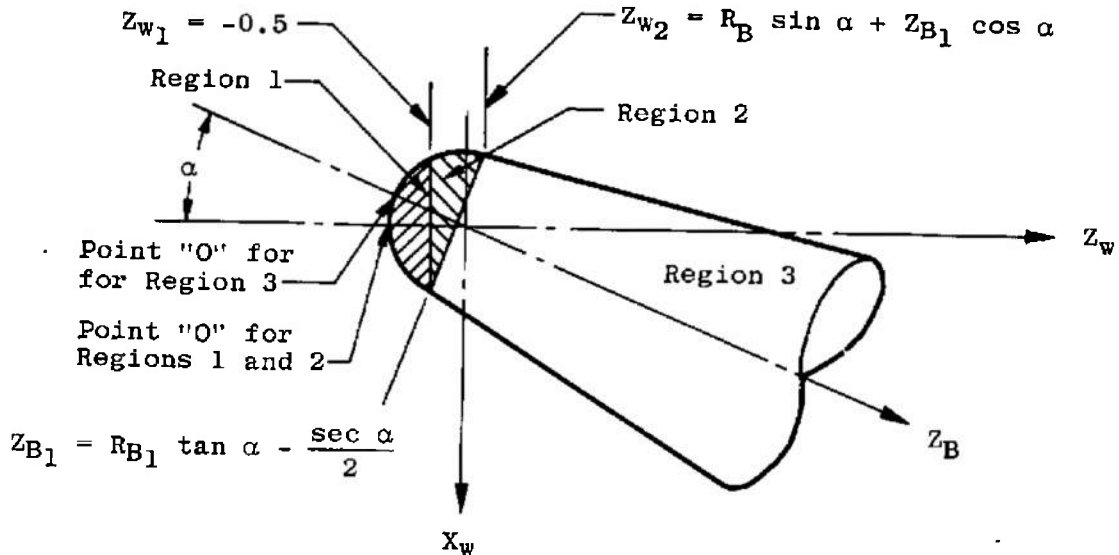
FORCE COEFFICIENTS

A general expression for the resultant force coefficient attributable to the surface pressure is

$$C_{F_{\vec{n}}} = \int_A \int C_p \vec{n} \, dA / \pi R_b^2 \quad (6)$$

where πR_b^2 is the reference base area, C_p the local pressure coefficient, and \vec{n} the local inward unit normal vector for an element of surface area, dA . As can be readily seen, the normal vector and the elemental area are functions of the local geometry, so that for the present case Eq. (6) was evaluated for two regions--the spherical cap

and the conical afterbody. However, for ease of computing, three regions were chosen, as shown in the following sketch.



In regions 1 and 2, the integration was performed in the wind-fixed axis system because these regions represented a sphere at zero angle of attack. So that for a given Z_w , C_p was constant, i. e., $C_p \neq f(\theta_\infty)$. Immediately, in region 1

$$\left(C_{Fz_w}\right)_t = -(2/Rb^2) \int_{-1}^{z_{w1}} C_p Z_w dZ_w \quad (7)$$

In region 1, the net effect of the forces acting in the X_w or Y_w direction was zero.

The resulting equations for region 2 are different only because of the lower limit of integration formed by the plane Z_{B_1} ; that is, the range of integration over θ_w was $+\theta_{w_1}$ to $-\theta_{w_1}$. For given Z_w and Z_{B_1} , one obtains

$$\theta_{B_1} = \cos^{-1} [(Z_w - Z_{B_1} \cos \alpha) / -R_{B_1} \sin \alpha]$$

where

$$R_{B_1} = \sqrt{1 - Z_{B_1}^2}$$

and

$$\theta_{w_1} = \tan^{-1} [R_{B_1} \sin \theta_{B_1} / (R_{B_1} \cos \theta_{B_1} \cos \alpha + Z_{B_1} \sin \alpha)]$$

Because of symmetry, the following equations result in region 2:

$$\left. \begin{aligned} (C_{FZ_w})_2 &= -(2/\pi R_b^2) \int_{Z_{w_1}}^{Z_{w_2}} C_p Z_w \theta_{w_1} dZ_w \\ (C_{FX_w})_2 &= (2/\pi R_b^2) \int_{Z_{w_1}}^{Z_{w_2}} C_p \sqrt{1 - Z_w^2} \sin \theta_{w_1} dZ_w \end{aligned} \right\} \quad (8)$$

In region 1, the values of C_p were taken from the blunt body (inverse) solution, which was used to compute the initial data for the GASL supersonic solution (region 3). In region 2, the solution obtained from the GASL program was used. In region 3, $C_p = C_p(\theta_w, Z_w) = C_p(\theta_B, Z_B)$, and from a geometrical view the equations are more tractable in the body-fixed axis system. The expression for the inward unit normal vector in the body-fixed axis system at any point on the cone was substituted into Eq. (6), and the integration performed with the result that

$$\left. \begin{aligned} (C_{F_{Z_B}})_3 &= (2 \tan \sigma_c / \pi R_b^2) \int_{Z_{B_1}}^{Z_{B_{max}}} R_B(Z_B) \int_c^{\theta_{B_{max}}} C_p(\theta_B, Z_B) d\theta_B dZ_B \\ (C_{F_{X_B}})_3 &= -(2/\pi R_b^2) \int_{Z_{B_1}}^{Z_{B_{max}}} R_B(Z_B) \int_c^{\theta_{B_{max}}} C_p(\theta_B, Z_B) \cos \theta_B d\theta_B dZ_B \end{aligned} \right\} \quad (9)$$

In this region, the GASL results were interpolated for a selected Z_B , the integrals over θ_B evaluated by the trapezoidal rule, and the results were then integrated over Z_B by the trapezoidal rule. Because of the large number of Z_B planes (150), this technique was considered to be sufficiently accurate. Because of symmetry, in all three regions the side forces integrate to zero.

MOMENT COEFFICIENT

The general equation for the three moments about a point "O" may be expressed as

$$(\vec{C}_M)_O = \int_A \int \vec{r} \times C_p \vec{n} dA / \pi R_b^2 D_b \quad (10)$$

where \vec{r} is the radius vector from point "O". In regions 1 and 2, the point "O" was chosen as the nose of the sphere ($Z_w = -1$), so that

$$\left. \begin{aligned} (C_M)_{O,1} &= 0 \\ (C_M)_{O,2} &= (C_{F_{X_w}})_2 / D_b \end{aligned} \right\} \quad (11)$$

The latter result was obtained because the resultant moment arm of the forces in region 2 was unity. In region 3, the point "O" was taken as the intersection of Z_B with the sphere, so that

$$\begin{aligned} (C_M)_{O,3} &= -(2/\pi R_b^2 D_b) \int_{Z_{B_1}}^{Z_{B_{max}}} R_B \left[R_B \tan \sigma_c + Z_B + 1 \right] \times \\ &\quad \int_c^{\theta_{B_{max}}} C_p(\theta_B, Z_B) \cos \theta_B d\theta_B dZ_B \end{aligned} \quad (12)$$

To add all the contributions of the various regions, the coefficients in regions 1 and 2 were transformed to region 3 through the angle of attack, so that the following expressions were obtained for the axial-force, normal-force, and pitching-moment coefficients and center of pressure location from the nose:

$$\left. \begin{aligned} C_A &= \left[(C_{F_{Z_w}})_1 + (C_{F_{Z_w}})_2 \right] \cos \alpha + (C_{F_{X_w}})_2 \sin \alpha + (C_{F_{Z_B}})_3 \\ C_N &= \left[(C_{F_{Z_w}})_1 + (C_{F_{Z_w}})_2 \right] \sin \alpha - (C_{F_{X_w}})_2 \cos \alpha - (C_{F_{X_B}})_3 \\ C_{m_{nose}} &= (C_m)_{0,3} + \left[(C_{F_{X_w}})_2 \cos \alpha - (C_{F_{Z_w}})_2 \sin \alpha \right] / D_b \\ Z_{cp}/D_b &= C_m / C_N \end{aligned} \right\} \quad (13)$$

Also

$$\left. \begin{aligned} C_L &= C_N \cos \alpha - C_A \sin \alpha \\ C_D &= C_A \cos \alpha + C_N \sin \alpha \end{aligned} \right\} \quad (14)$$

and

$$L/D = C_L / C_D \quad (15)$$

These final equations with the results from the GASL program were used to compute the force and moment coefficients for comparison with the experimental data.

NEWTONIAN THEORY

The pressure coefficient from modified Newtonian theory is

$$C_p = C_{p_0} \cos^2 \eta \quad (16)$$

where C_{p_0} is the pressure coefficient at the forward stagnation point on a blunt body. A value of 1.841 was used for C_{p_0} in these computations which corresponds to the normal-shock pressure for $M = 18$. The angle η is the acute angle between the free-stream velocity vector and the local unit normal vector, i. e.

$$\cos \eta = \vec{V} \cdot \vec{n} / |\vec{V}|$$

Thus

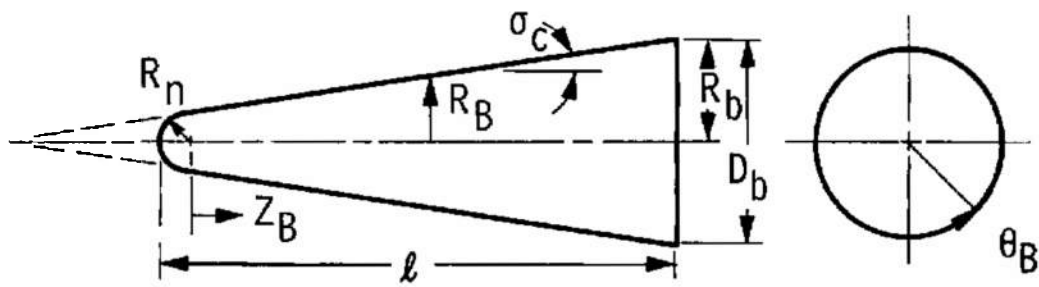
$$C_p = 1.841 (\vec{V} \cdot \vec{n} / |\vec{V}|)^2 \quad (17)$$

was used to predict the surface pressure distribution. The value of C_p was substituted into the force equations, and the Newtonian force coefficients were computed. One precept of the modified Newtonian theory is that the pressure is zero in a "shadowed" region. Thus, on integrating the pressure distribution, the limit was set at $\cos \eta = 0$, or $\eta = \pi/2$.

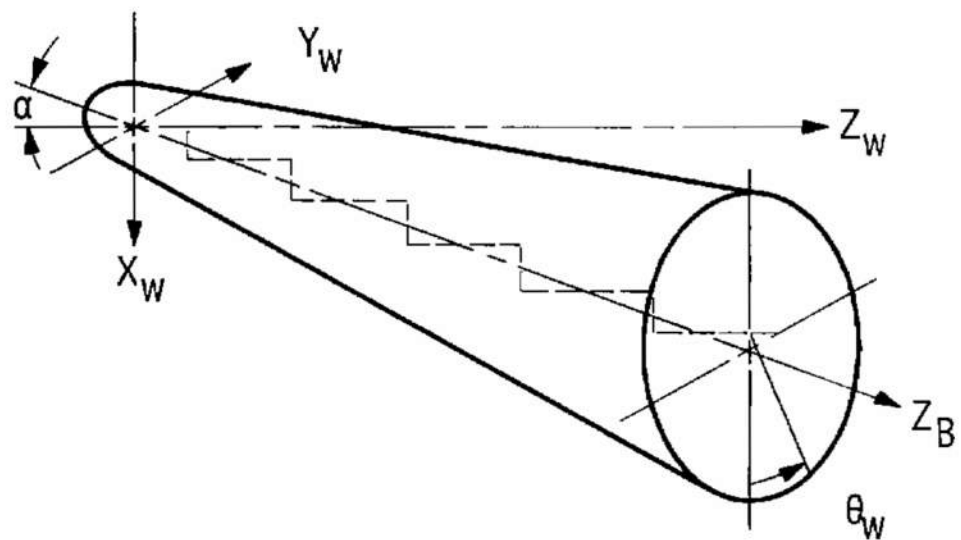
REFERENCES

1. Moretti, G., Sanlorenzo, E. A., Magnus, E. E., and Weilerstein, G. "Supersonic Flow about General Three-Dimensional Bodies: Flow Field Analysis of Reentry Configurations by a General Three-Dimensional Method of Characteristics, Vol. III." ASD-TDR-61-727, October 1962.
2. Jenkins, B. Z. "Real Gas Flow Field Properties around Blunt Cones, Vol. I." U. S. Army Missile Command Rept. No. RF-TR-63-18, August 1963.
3. Whitfield, Jack D. and Griffith, B. J. "Viscous Effects on Zero-Lift Drag of Slender Blunt Cones." AEDC-TDR-63-35, March 1963. See also AIAA Journal, Vol. 2, No. 10, October 1964, pp. 1714-1722.
4. Griffith, B. J. and Lewis, C. H. "Laminar Heat Transfer to Spherically Blunted Cones at Hypersonic Conditions." AIAA Journal, Vol. 2, No. 3, March 1964, p. 438.
5. Lewis, Clark H. and Whitfield, J. D. "Theoretical and Experimental Studies of Hypersonic Viscous Effects." Paper presented at the AGARD Specialists' Meeting, Naples, Italy, May 1965, AGARDograph 97, Part III, also AEDC-TR-65-100 (AD 462717), May 1965.
6. Sanlorenzo, E. and Petri, F. "Programs for the Analyses of Flow Fields around Spherically Capped Three-Dimensional Bodies at Angles of Attack." GASL-TR-462, September 1964.
7. Edenfield, E. E. "Comparison of Hotshot Tunnel Force, Pressure, Heat Transfer and Shock Shape Data with Shock Tunnel Data." AEDC-TDR-64-1 (AD 428916), January 1964.
8. Wilkinson, David B. and Harrington, Shelby A. "Hypersonic Force, Pressure, and Heat Transfer Investigations of Sharp and Blunt Slender Cones." AEDC-TDR-63-177 (AD 414616), August 1963.
9. Cheng, H. K. "Hypersonic Flow with Combined Leading-Edge Bluntness and Boundary-Layer Displacement Effect." Cornell Aeronautical Lab Report AF-1285-A-4 (AD 243140), August 1960.
10. Whitfield, Jack D. and Griffith, B. J. "Viscous Drag Effects on Slender Cones in Low-Density Hypersonic Flow." Submitted for Publication in AIAA Journal.

11. Whitfield, Jack D. and Wolny, W. "Hypersonic Static Stability of Blunt Slender Cones." AEDC-TDR-62-166 (AD 282897), August 1962.
12. Harris, Julius E. "Force-Coefficient and Moment-Coefficient Correlations and Air-Helium Simulation for Spherically Blunted Cones." NASA-TN-D-2184, November 1964.



a. Cone Nomenclature



b. Cone Coordinate Systems

Fig. 1 Cone Nomenclature and Coordinate Systems

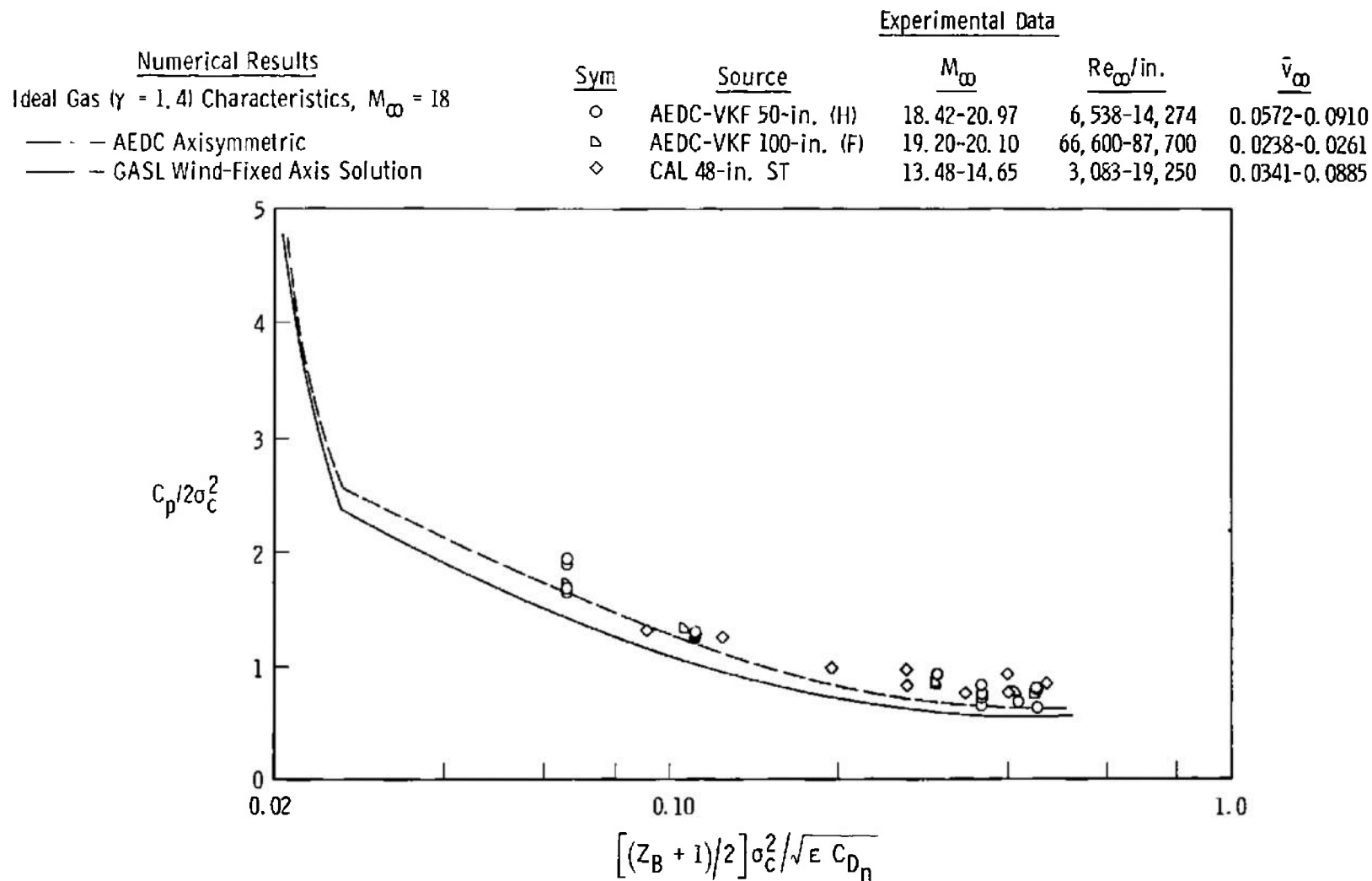
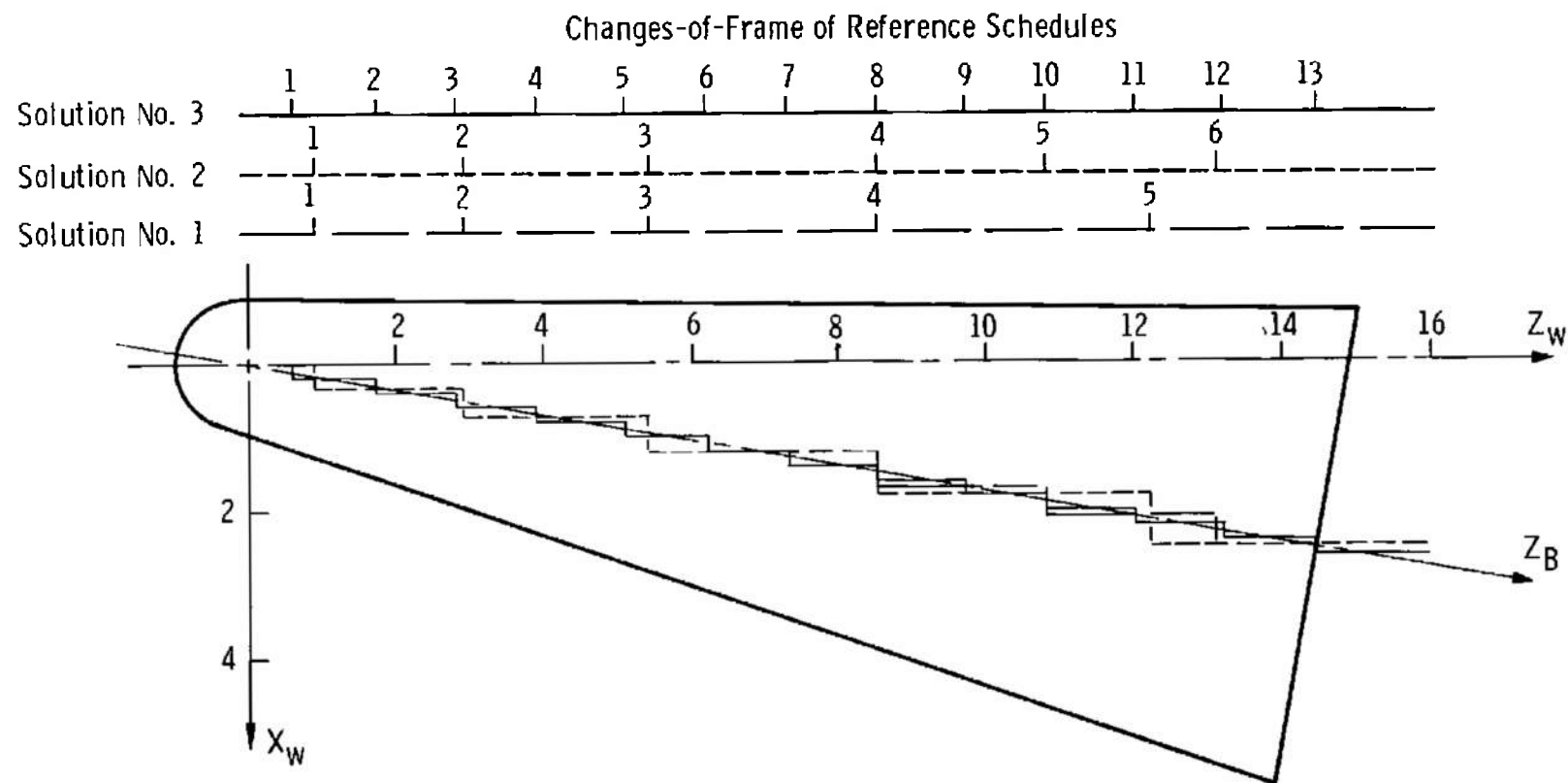


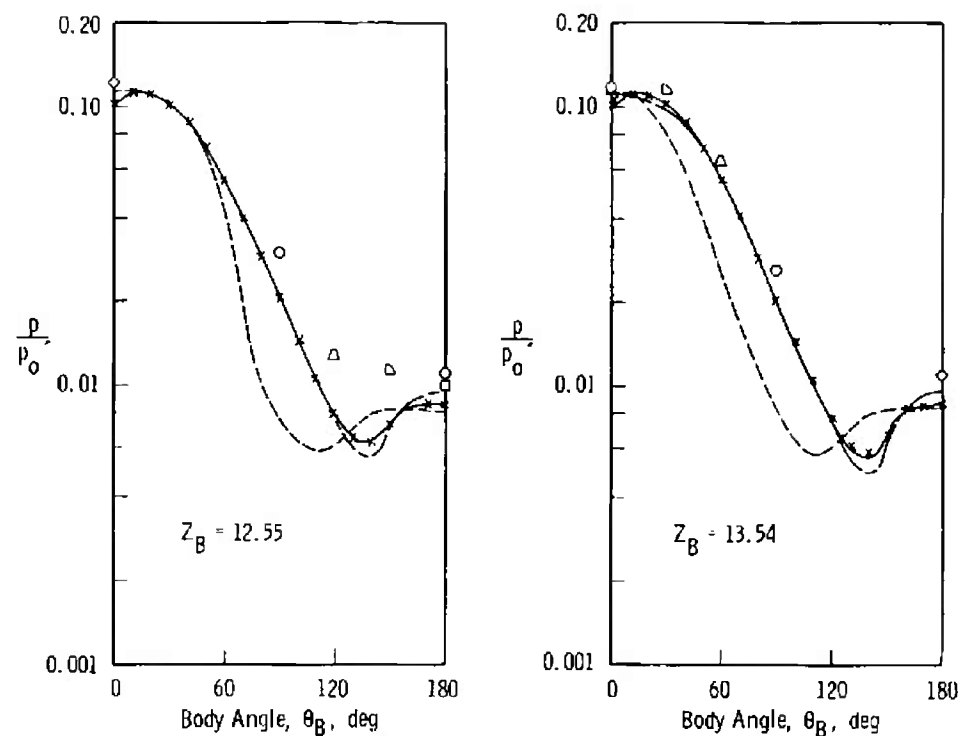
Fig. 2 Zero-Lift Pressure Distribution over 9-deg Half-Angle Spherically Blunted Cones



a. Three Scheduled Changes-of-Frame

Fig. 3 Effects of Changes-of-Frame on Body Pressures at $\alpha = 10$ deg

Numerical Results		Experimental Data				
Ideal Gas ($\gamma = 1.4$), $M_\infty = 18$		Sym	Source	Run	M_∞	Re_∞ /in.
---	GASL Wind-Fixed Axis Solution No. 1	○	AEDC-VKF 50-in. (H)	1367	18.45	8,313
---	GASL Wind-Fixed Axis Solution No. 2	□	AEDC-VKF 50-in. (H)	1368	21.57	4,526
*****	GASL Wind-Fixed Axis Solution No. 3	◇	AEDC-VKF 50-in. (H)	1372	18.97	13,140
---	GASL Body-Fixed Axis Solution	▷	AEDC-VKF 50-in. (H)	1379	18.99	9,320
		△	AEDC-VKF 50-in. (H)	1380	19.37	13,433
		○	AEDC-VKF 50-in. (H)	1381	18.89	11,046
						\bar{v}_∞
						0.0710
						0.1125
						0.0581
						0.0691
						0.0585
						0.0631



b. Radial Pressure Distributions for Three Change-of-Frame Schedules

Fig. 3 Concluded

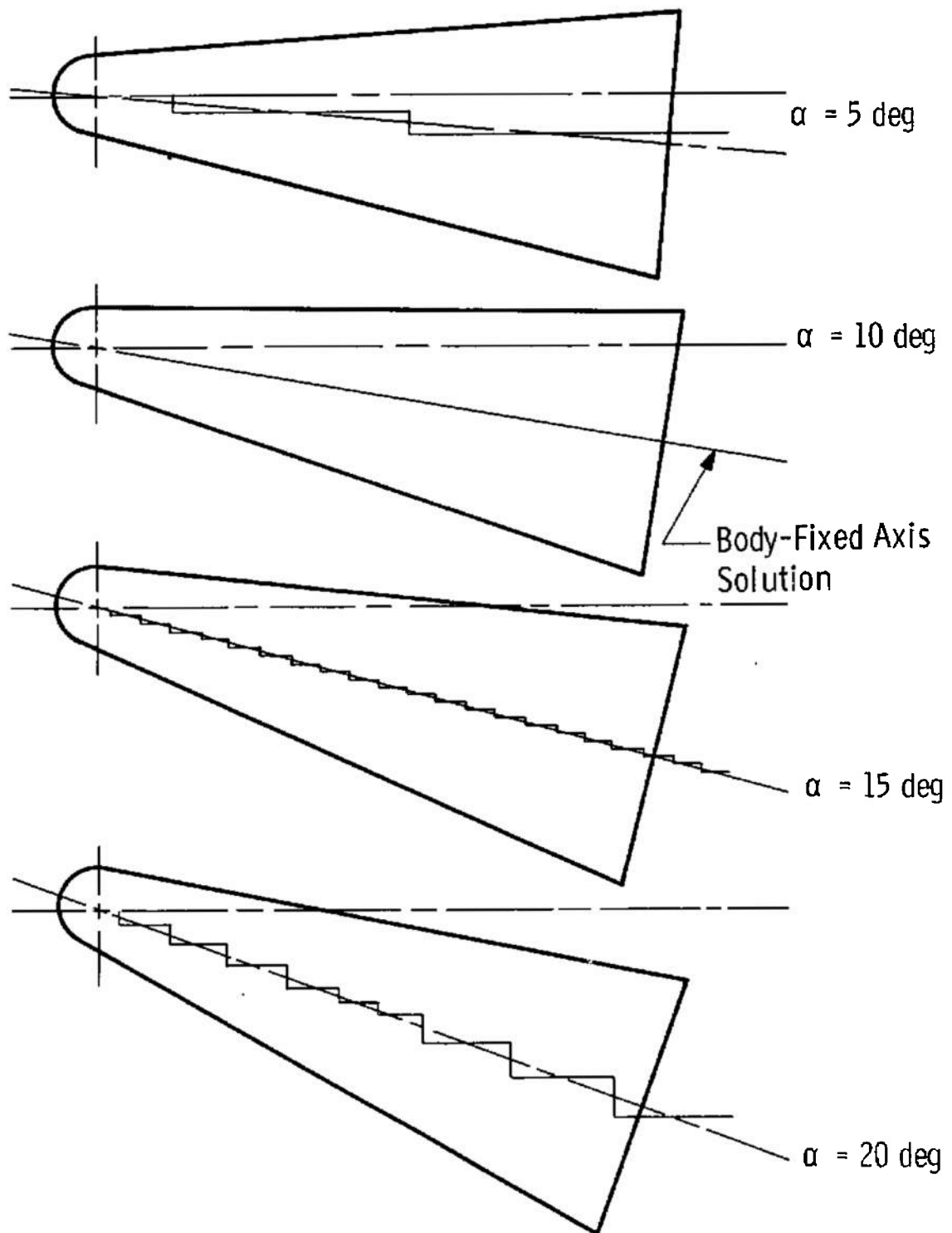


Fig. 4 Scheduled Changes-of-Frame for Various Angles of Attack

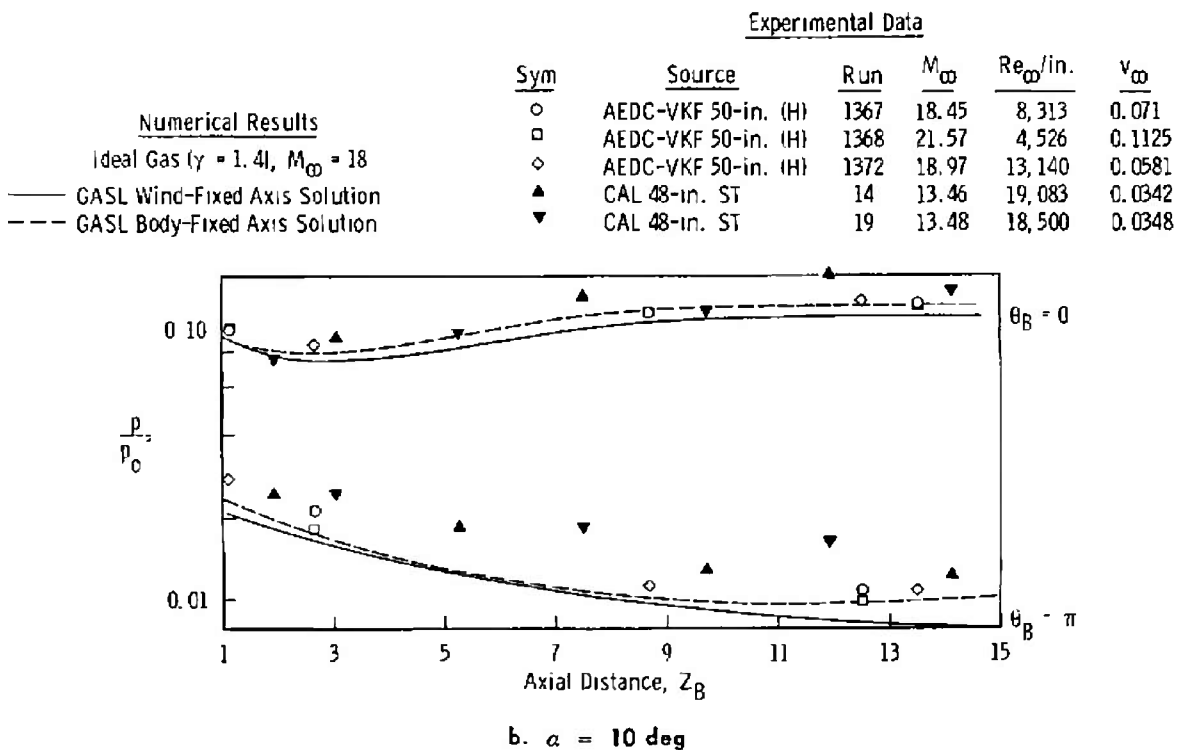
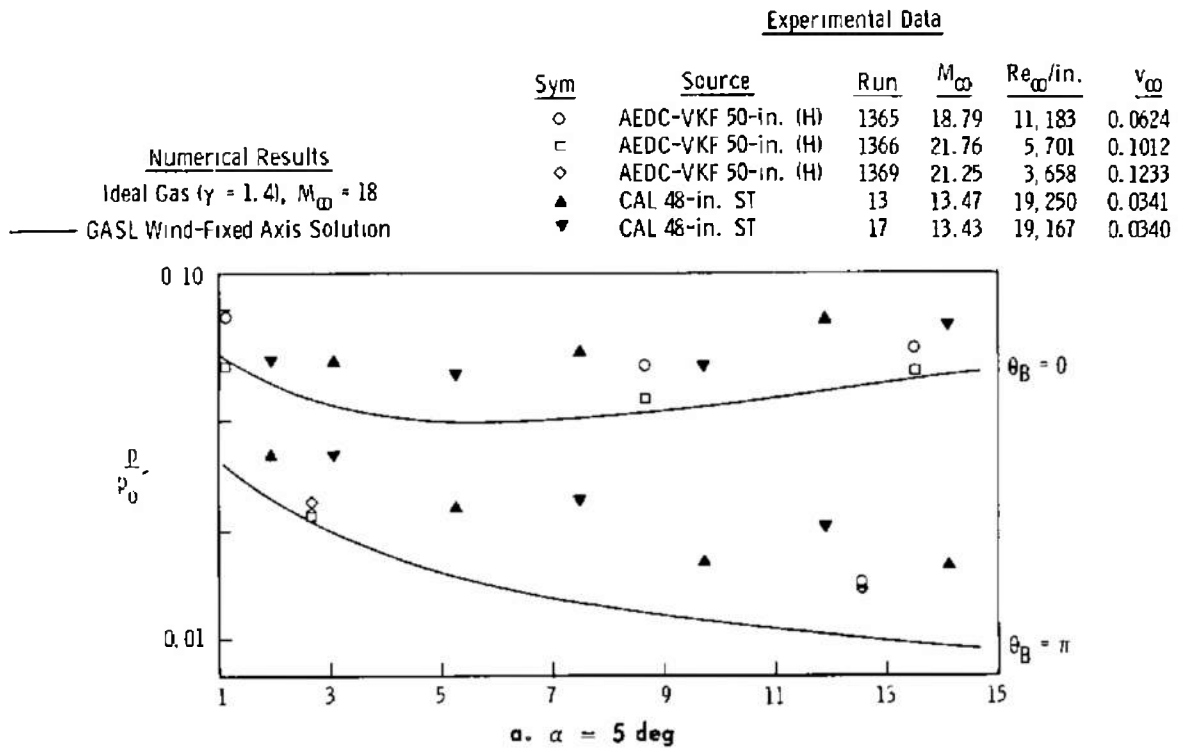
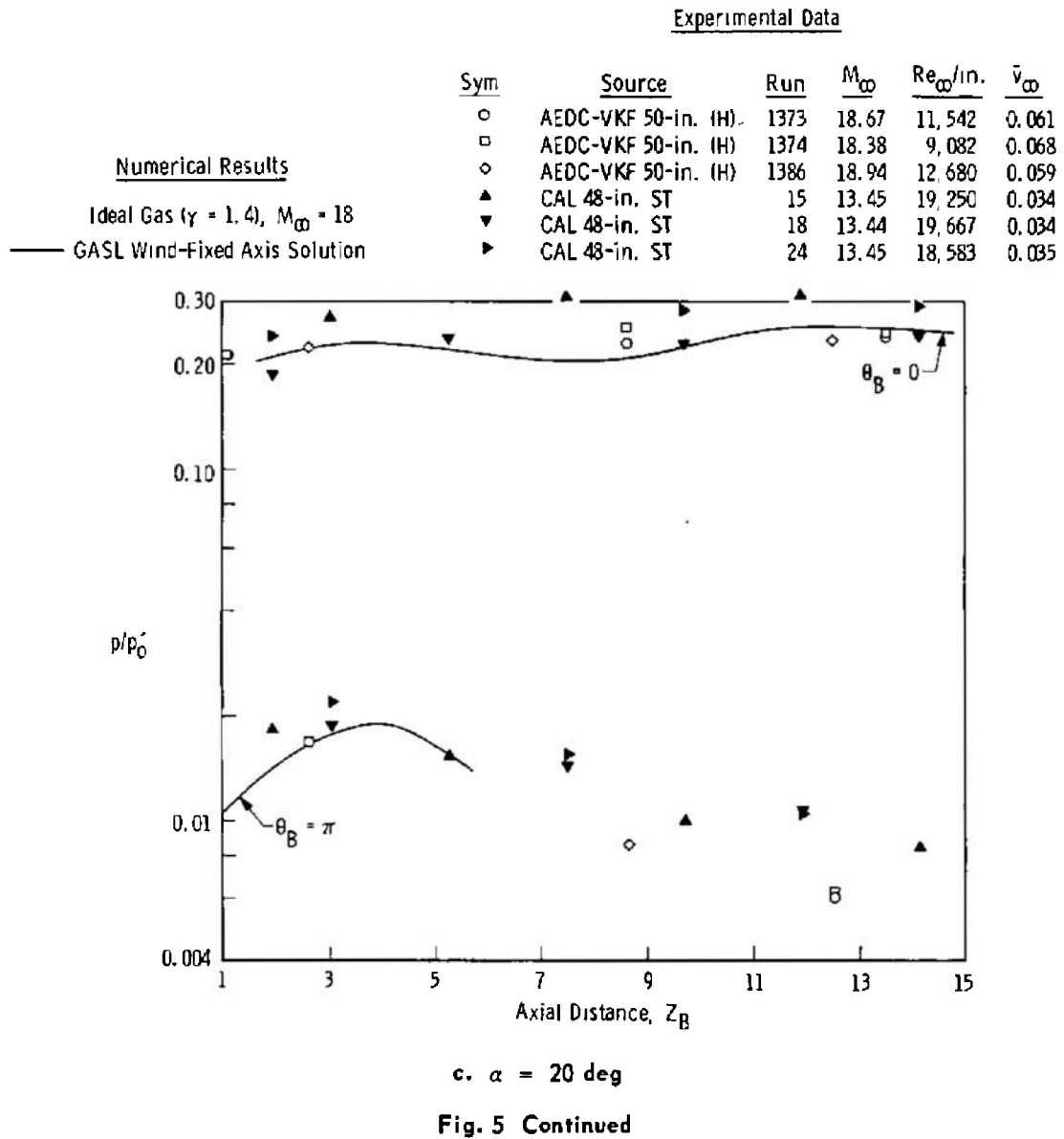
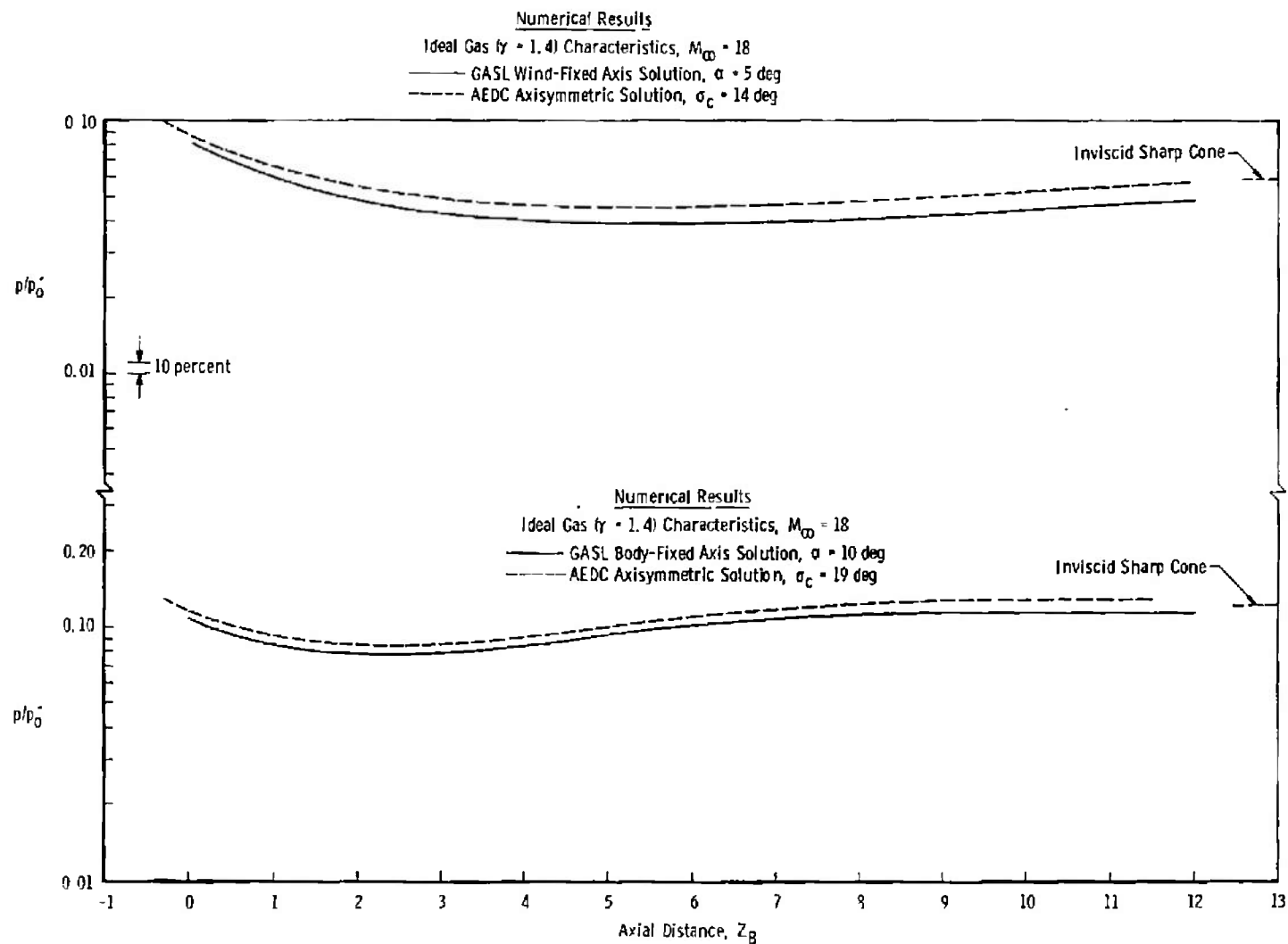


Fig. 5 Pressure Distributions along Most Windward and Leeward Streamlines at $M_\infty = 18$ and at Angles of Attack





d. Windward-Streamline Pressure Distribution from GASL ($\alpha = 5$ and $\alpha = 10$ deg)
and AEDC Axisymmetric "Equivalent" Cone Solutions

Fig. 5 Concluded

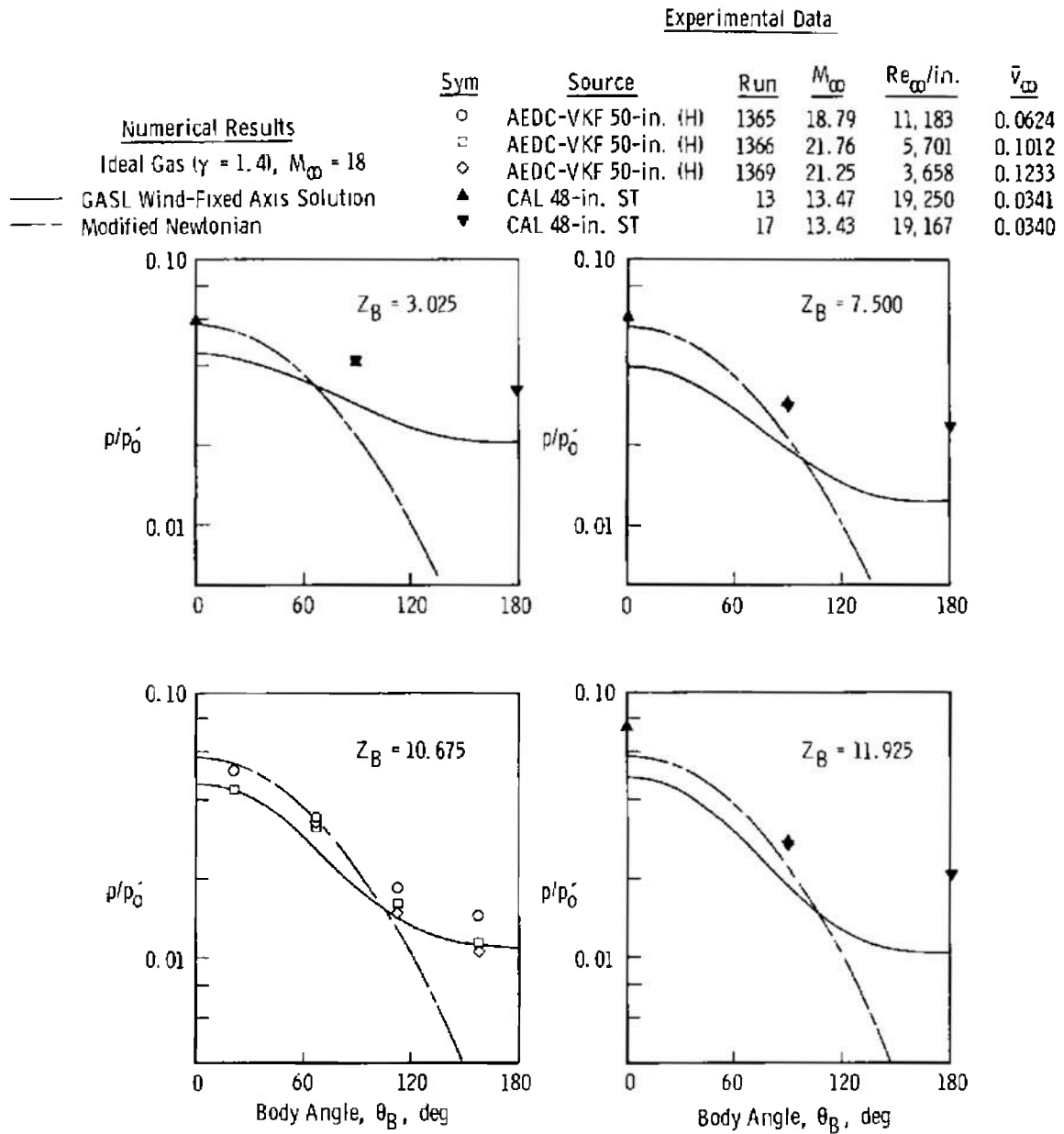


Fig. 6 Radial Pressure Distributions over a 9-deg Half Angle Spherically Blunted Cone at $M_\infty = 18$ and $\alpha = 5^\circ$

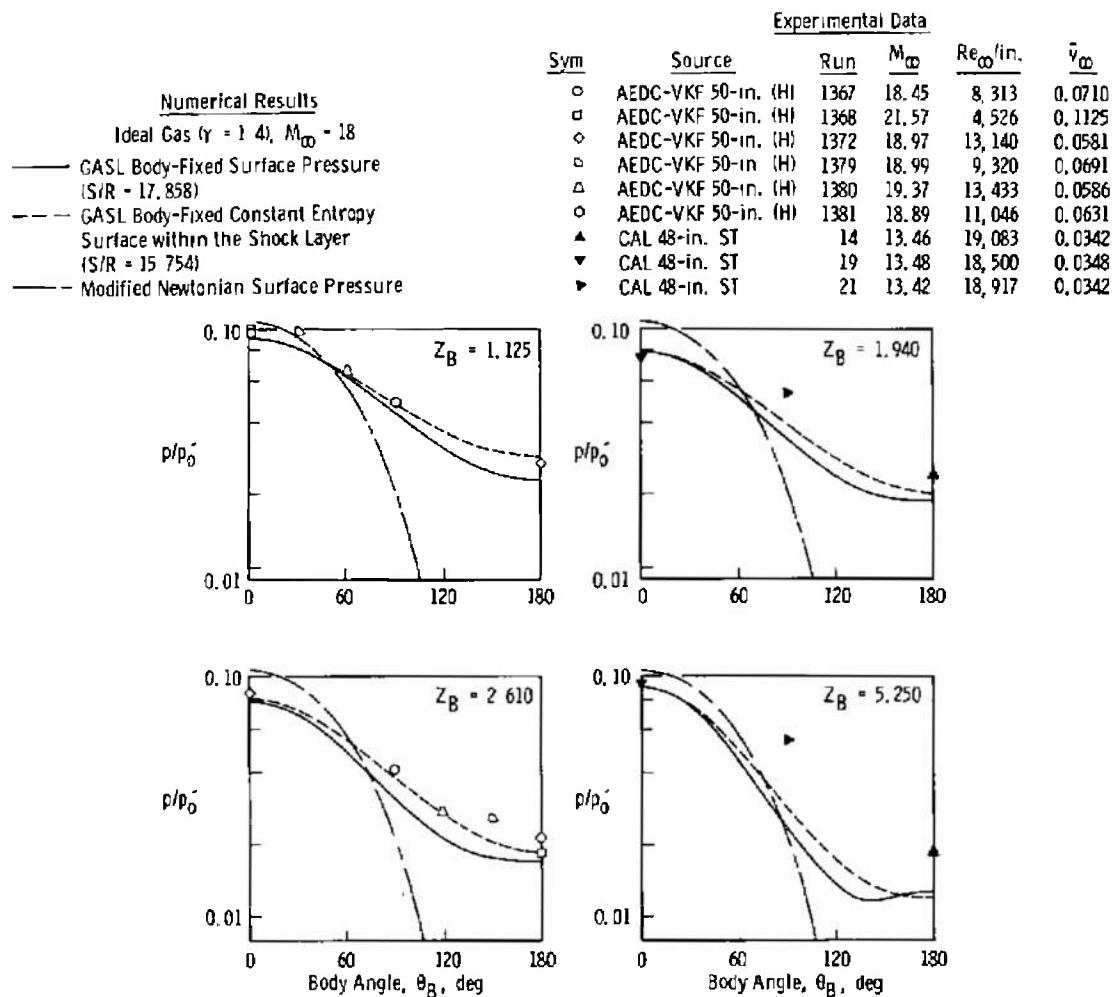


Fig. 7 Radial Pressure Distributions over a 9-deg Half-Angle Spherically Blunted Cone at $M_\infty = 18$ and $\alpha = 10$ deg

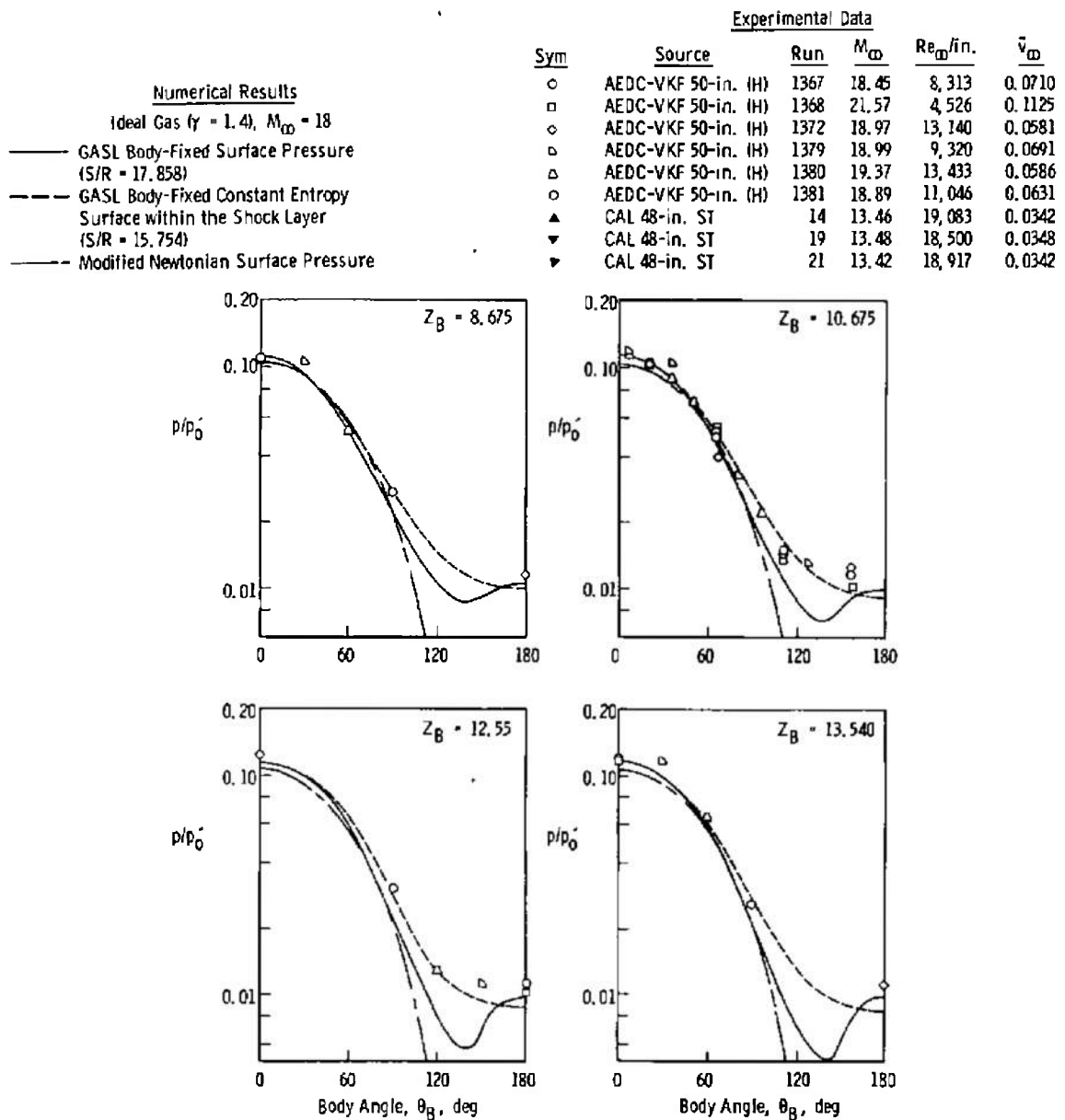


Fig. 7 Concluded

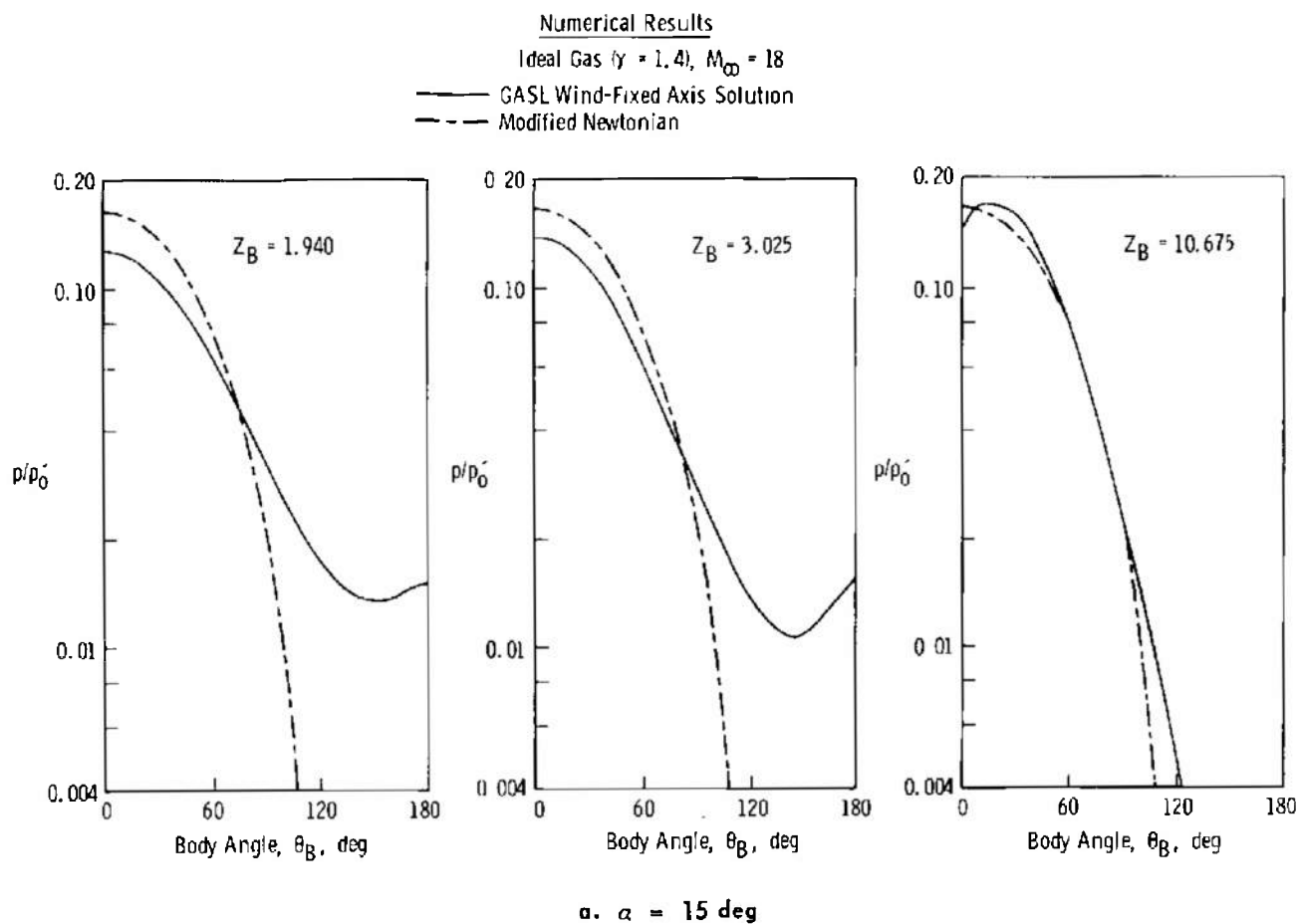


Fig. 8 Radial Pressure Distributions over a 9-deg Half-Angle Spherically Blunted Cone at $M_\infty = 18$ and at Angle of Attack

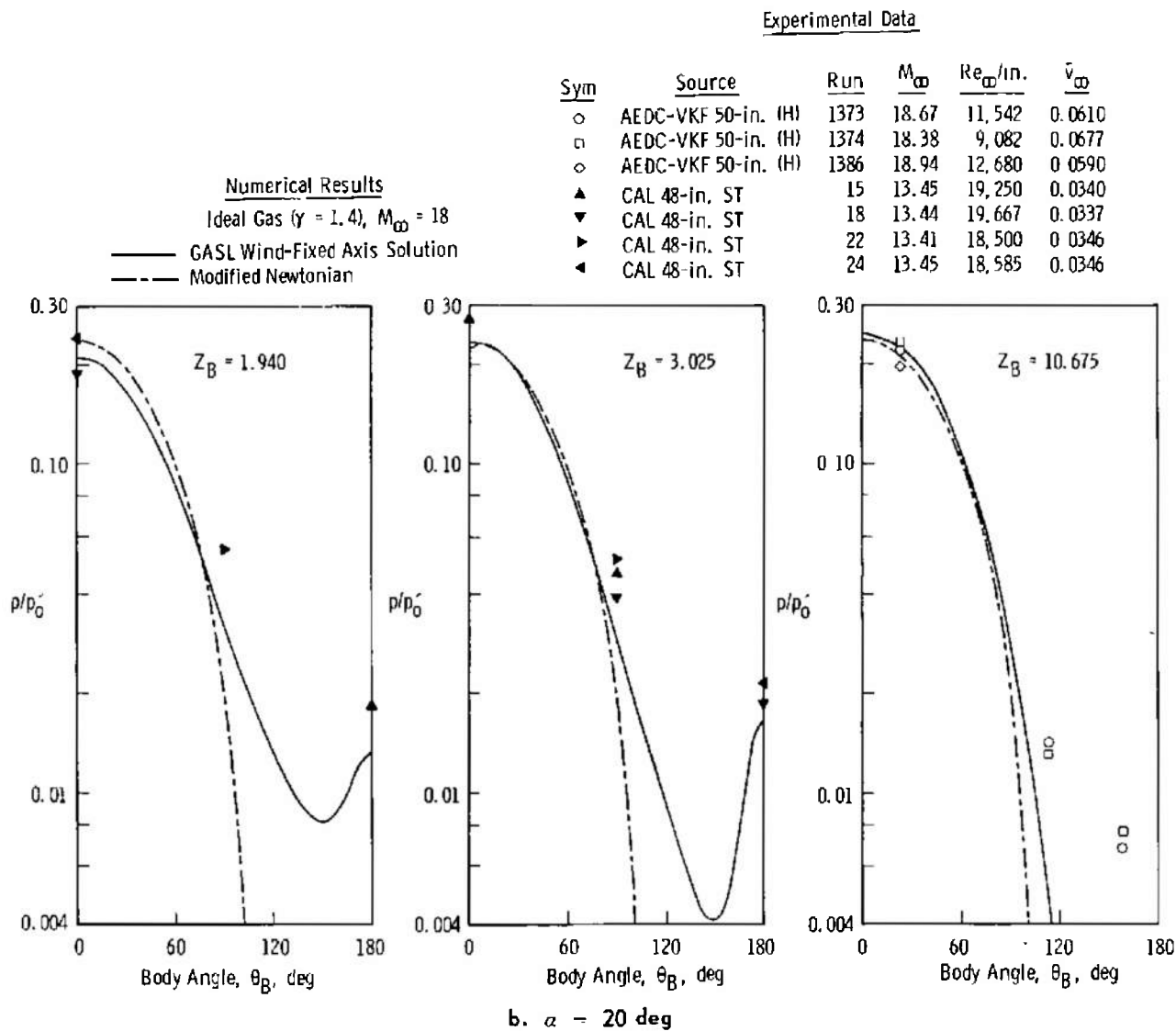


Fig. 8 Concluded

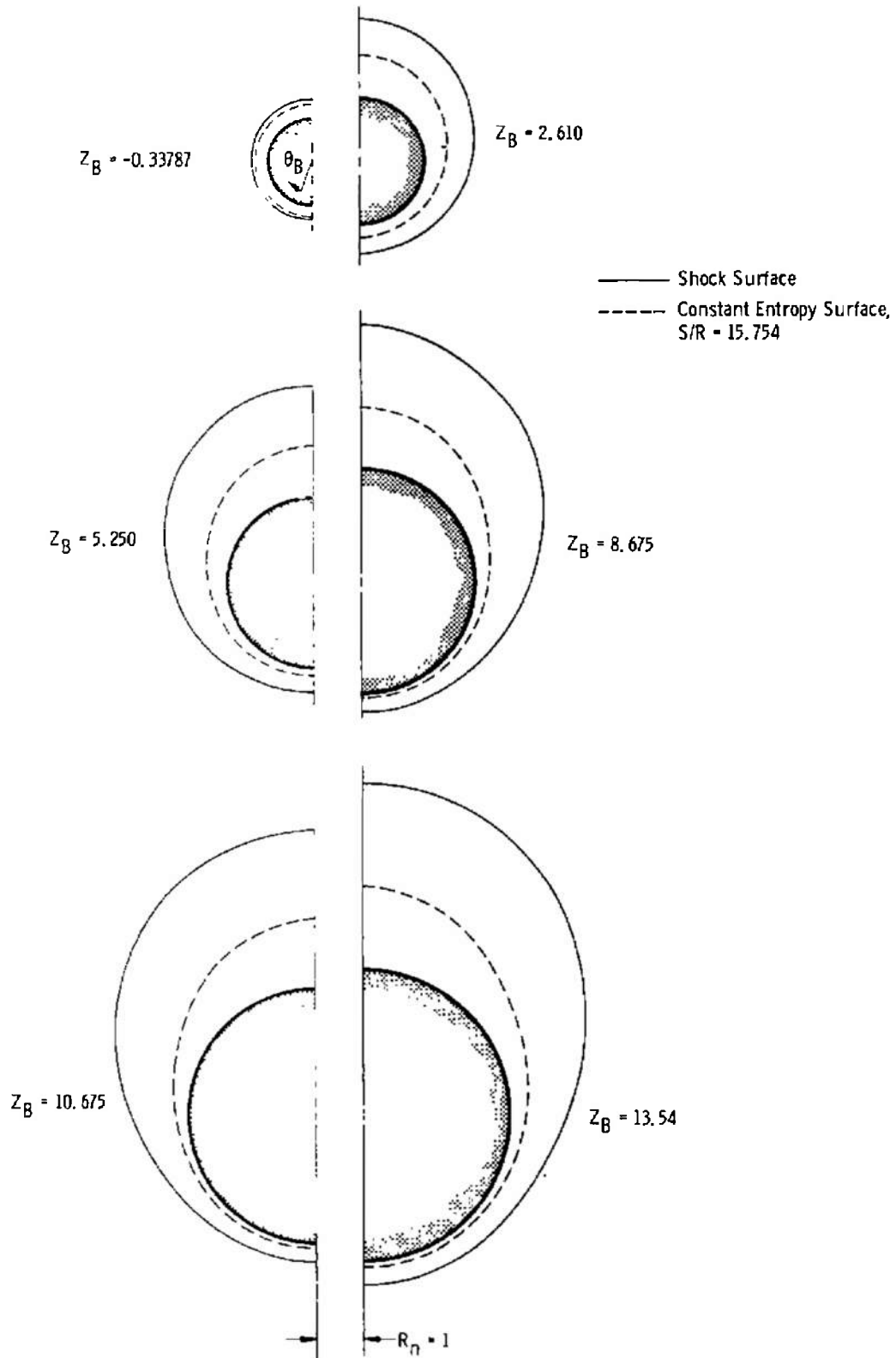
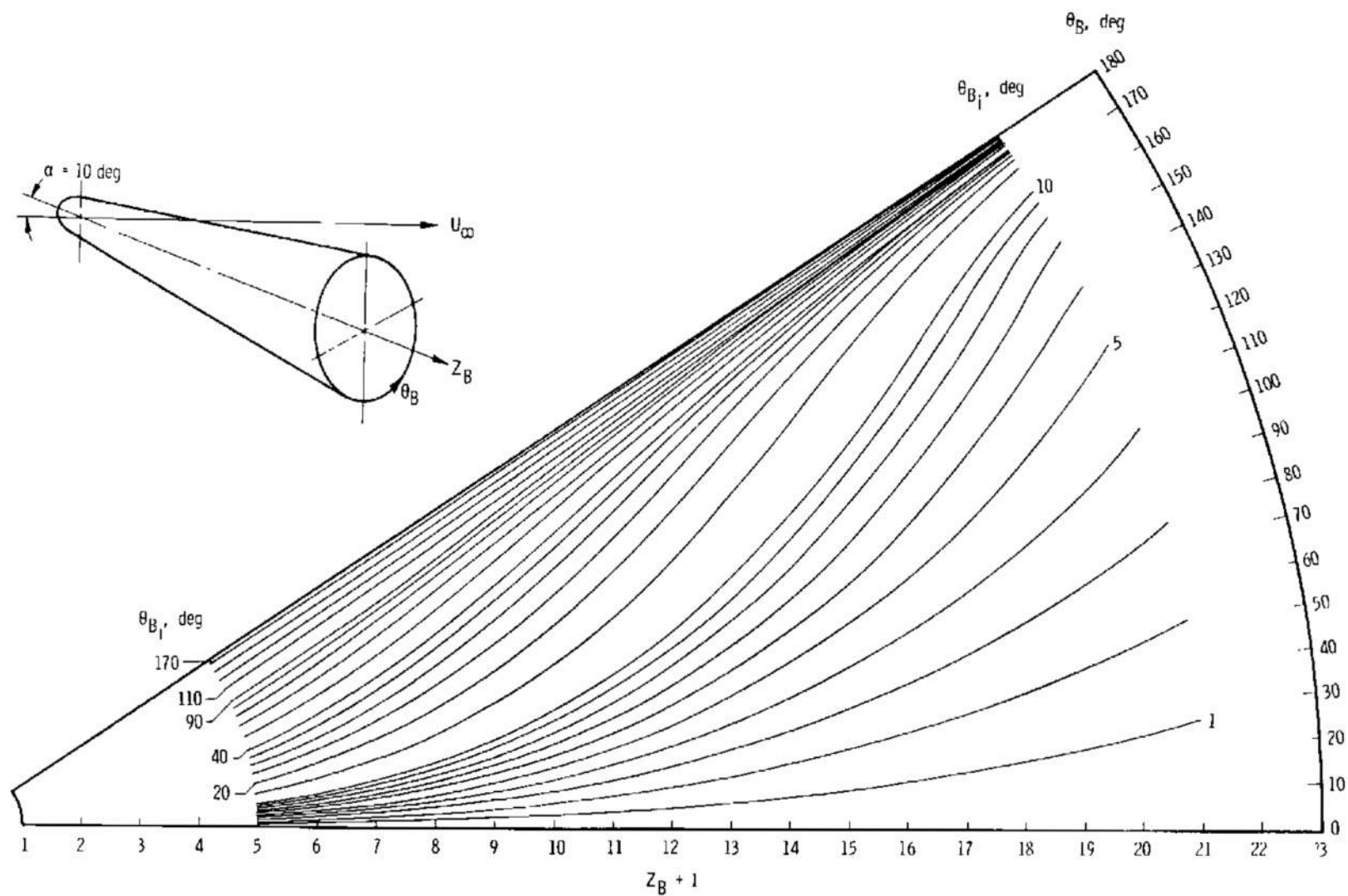
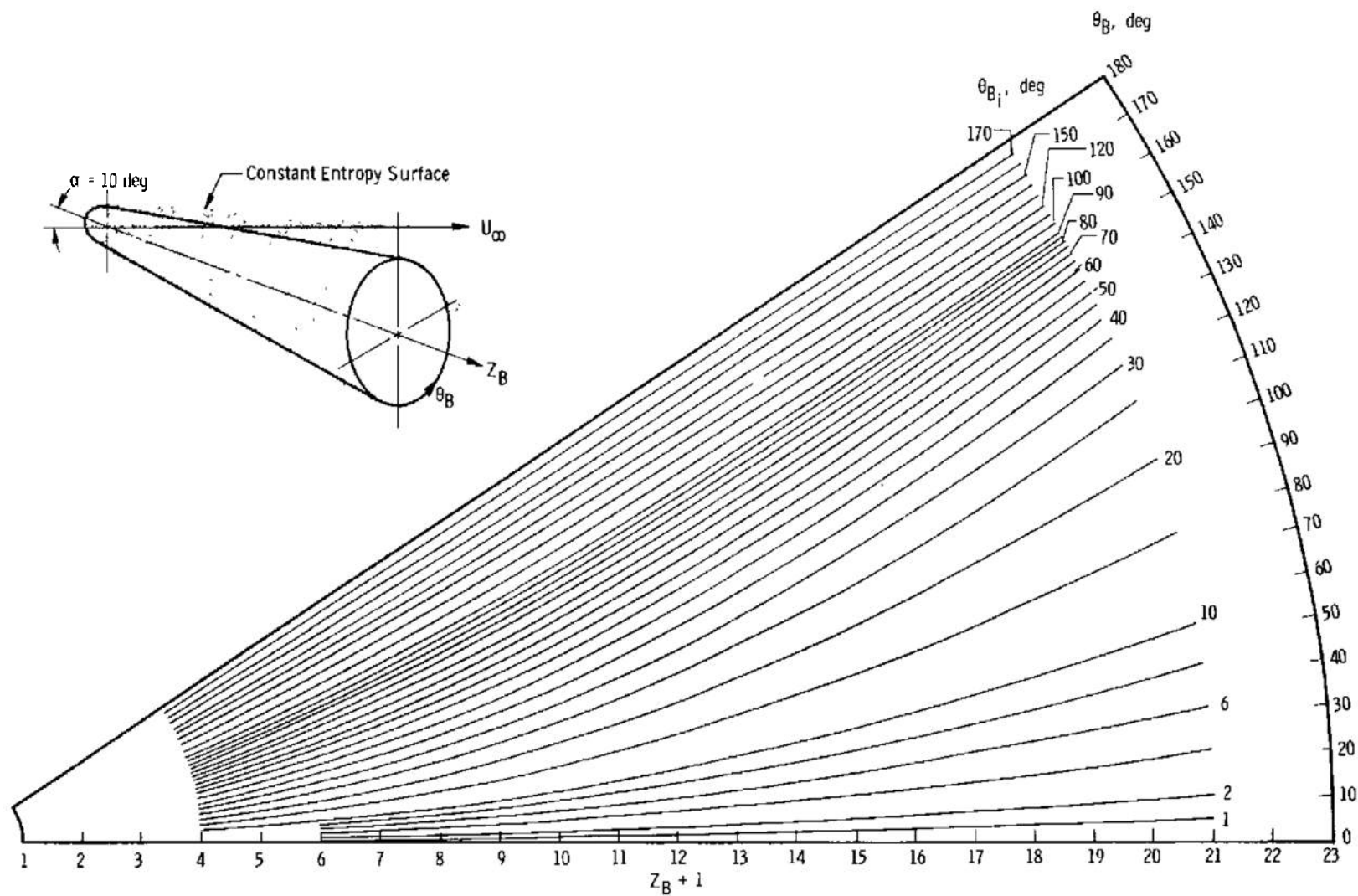


Fig. 9 Radial Cross Sections of Shock and Constant Entropy Surfaces at Selected Stations (Z_B) versus Radial Angle (θ_B)



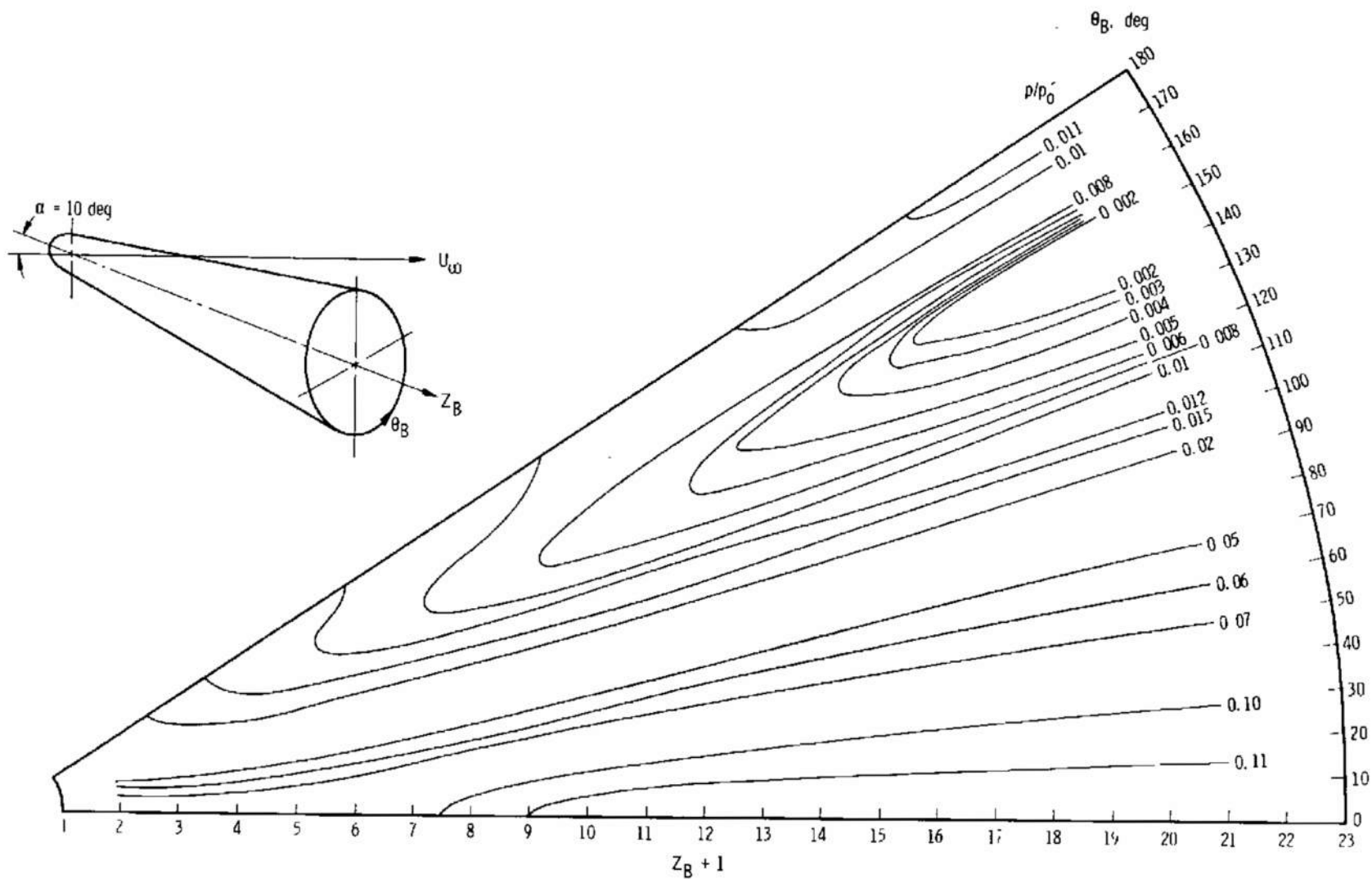
a. Body Surface ($S/R = 17.858$)

Fig. 10 Streamline Patterns for a 9-deg Half-Angle Cone at $\alpha = 10^\circ$ from the GASL Body-Fixed Axis Solution



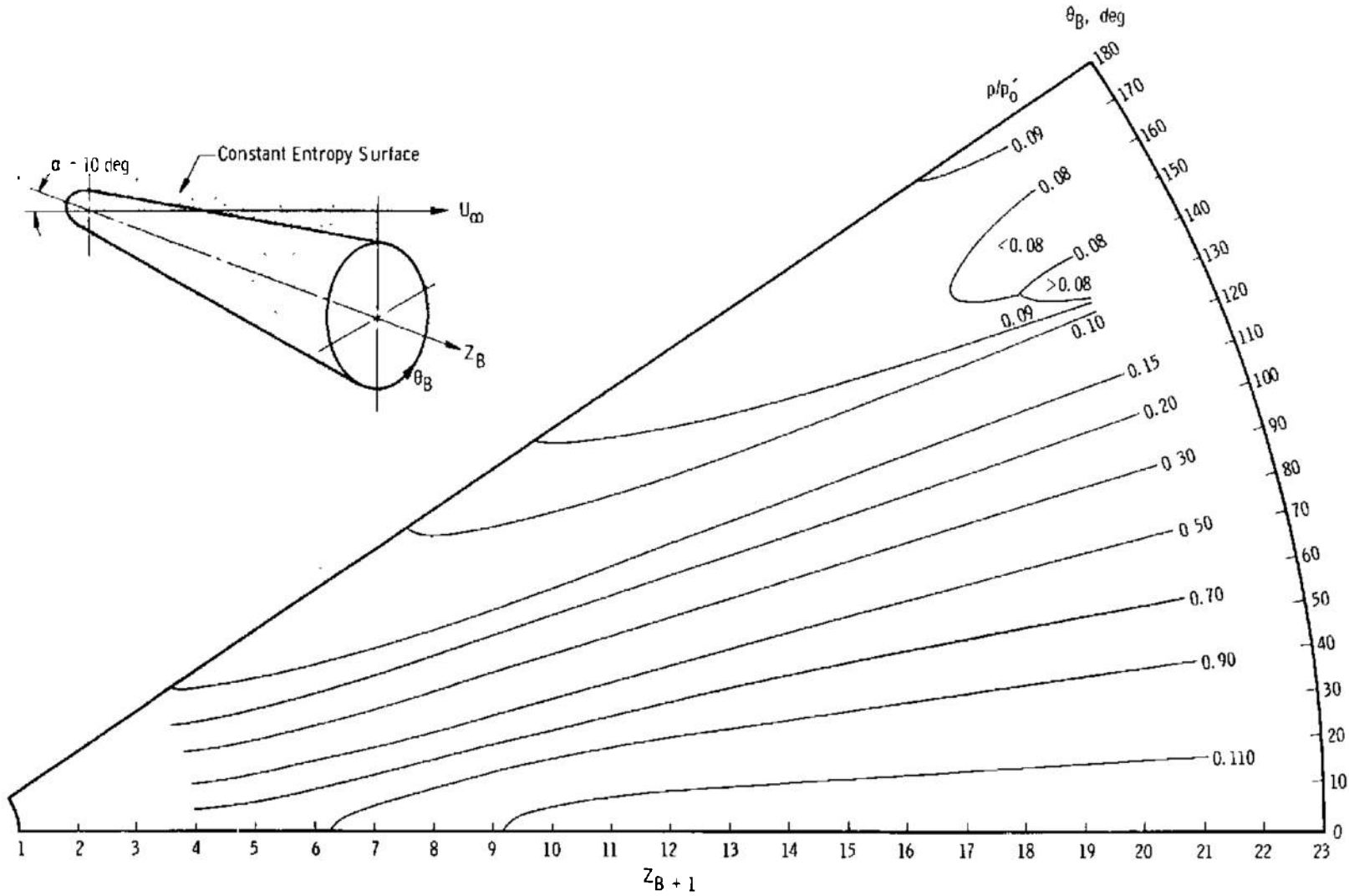
b. Constant Entropy Surface ($S/R = 15.754$)

Fig. 10 Concluded



a. Body Surface Isobars

Fig. 11 Pressure Contours for a 9-deg Half-Angle Cone at $\alpha = 10$ deg from the GASL Body-Fixed Axis Solution



b. Constant Entropy Surface Isobars

Fig. 11 Concluded

Numerical Results

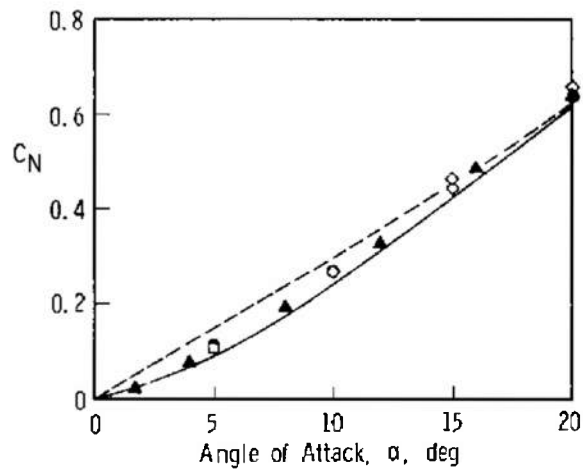
Ideal Gas ($\gamma = 1.4$), $M_\infty = 18$

Pressure Distribution from

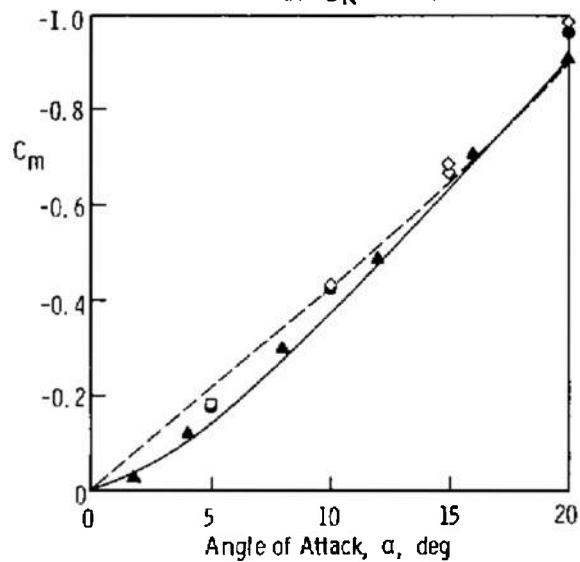
— GASL Wind-Fixed Axis Solution
 --- Modified Newtonian

Experimental Data

Sym	Source	M_∞	$Re_\infty/in.$	σ_c , deg	R_n/R_b	\bar{v}_∞	T_w/T_0
●	CAL 48-in. Shock Tunnel	14.7	14,000	9	0.3	~0.05	~0.1
□	AEDC-VKF 50-in. (H)	18.45	13,000	9	0.3	~0.05	~0.1
◇	AEDC-VKF 100-in. (F)	16.5-20	9,000-41,000	9	0.3	~0.05	~0.1
▲	NASA Helium Tunnel	19	200,000	10	0.255	~0.02	~1.0



a. C_N with α



b. C_m with α

Fig. 12 Force and Moment Coefficients for Spherically Blunted Cones at $M_\infty = 18$

Numerical ResultsIdeal Gas ($\gamma = 1.4$), $M_\infty = 18$

Pressure Distribution from

— GASL Wind-Fixed Axis Solution
 --- Modified Newtonian

Experimental Data

Sym	Source	M_∞	$Re_\infty/in.$	σ_c , deg	R_n/R_b	\bar{v}_∞	T_w/T_o
●	CAL 48-in. Shock Tunnel	14.7	14,000	9	0.3	~0.05	~0.1
□	AEDC-VKF 50-in. (H)	18.45	13,000	9	0.3	~0.05	~0.1
◇	AEDC-VKF 100-in. (F)	16.5-20	9,000-41,000	9	0.3	~0.05	~0.1
▲	NASA Helium Tunnel	19	200,000	10	0.255	~0.02	~1.0

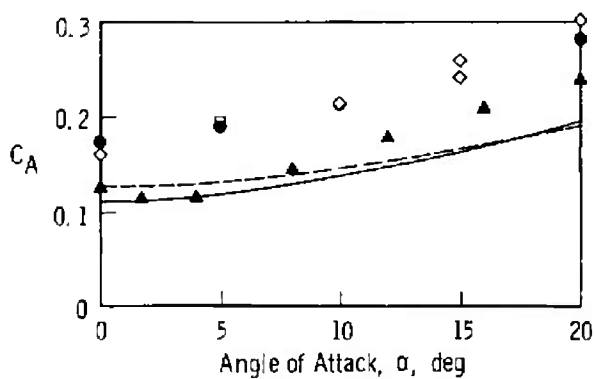
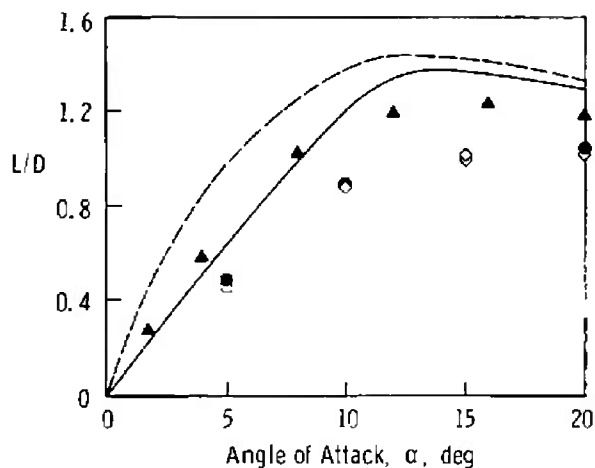
c. C_A with α d. Lift-to-Drag Ratio with α

Fig. 12 Concluded

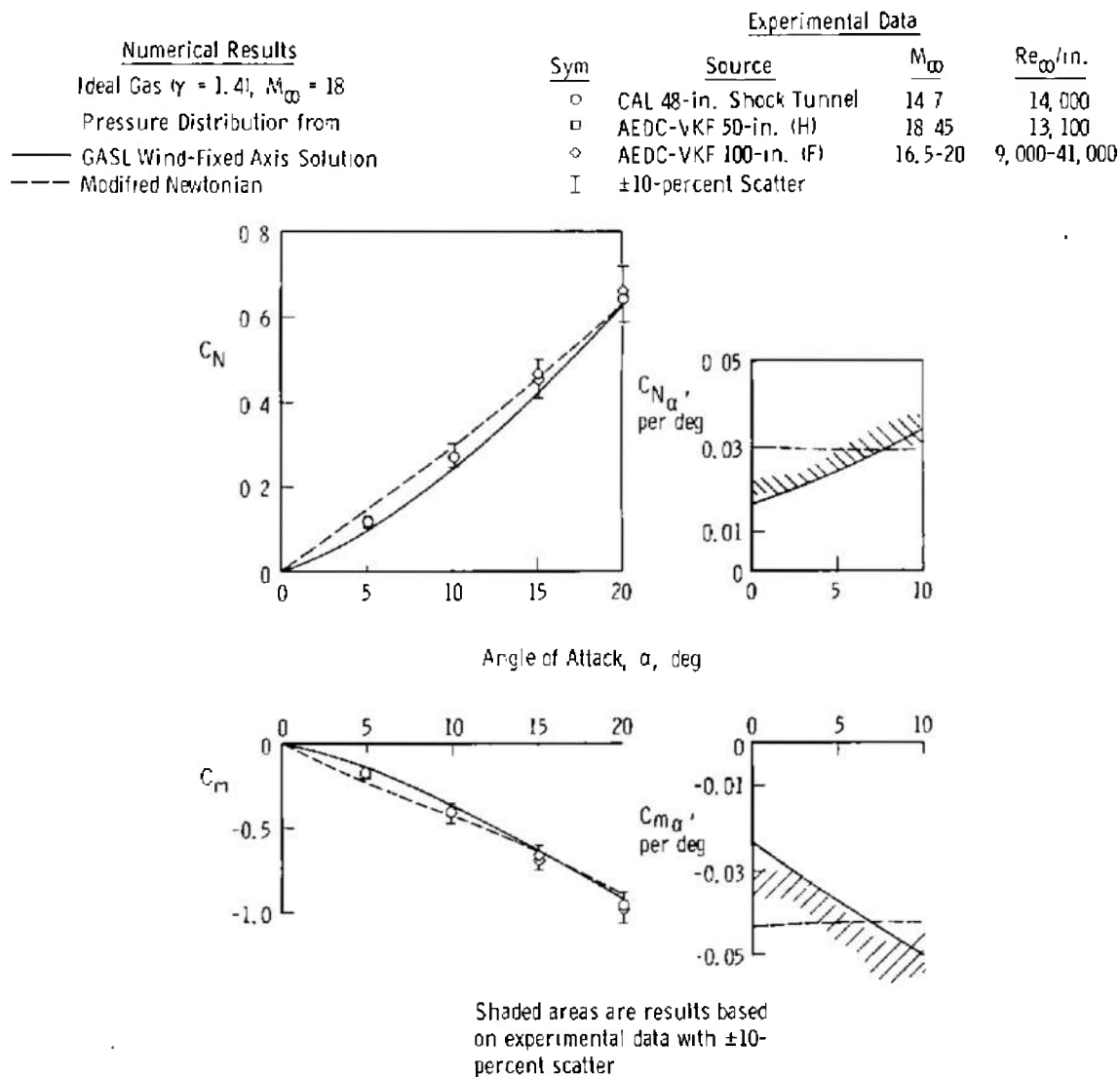


Fig. 13 Variation of Normal-Force and Pitching-Moment Coefficient Slopes with Angle of Attack for a 9-deg Half-Angle Spherically Blunted Cone at $M_\infty = 18$

TABLE I
PRESSURE DATA FROM AEDC-VKF TUNNELS

Surface Distance, s Axial Distance, Z _B Model Radial Angle, θ_B , deg				2.70 1.125 0	4.19 2.61 180	10.35 8.675 0	12.35 10.675 157.5	12.35 10.675 112.5	12.35 10.675 67.5	12.35 10.675 22.5	14.28 12.55 180	15.28 13.54 0	10.35 8.675 180
Tunnel	Run No.	Tunnel Angle of Attack	Tunnel Roll Angle	P/P ₀									
50-in. (H) ↓	1362*	0	0	0.0456	0.0360	0.0263	0.0212	0.0223	0.0249	0.0232	0.0227	0.0239	
	1363	0	0	0.0459	0.0345	0.0238	0.0195	0.0200	0.0221	0.0180	0.0200	0.0183	
	1364*	0	0	0.0521	0.0352	0.0249	0.0240	0.0220	0.0240	0.0229	0.0215	0.0232	
	1365*	5	0	0.0769	0.0212	0.0564	0.0142	0.0184	0.0340	0.0513	0.0143	0.0632	
	1366	5	0	0.0563	0.0220	0.0459	0.0113	0.0160	0.0312	0.0435	0.0140	0.0542	
	1367*	10	0	0.0965	0.0213	0.1110	0.0112	0.0147	0.0515	0.1087	0.0110	0.1200	
	1368	10	0	0.0978	0.0184	0.1100	0.0102	0.0131	0.0542	0.1016	0.0100	0.1180	
	1369	5	0	---	0.0240	---	0.0109	0.0148	0.0320	---	0.0137	---	
	1370*	0	0	0.0527	0.0362	0.0236	0.0216	0.0222	0.0238	0.0221	0.0216	0.0224	
	1372*	10	180	0.0278	0.0840	0.0113	0.1030	0.0393	0.0140	0.0122	0.1220	0.0110	
	1373*	20	0	0.2100	0.0150	0.2300	0.0067	0.0140	---	0.2200	0.0060	0.2400	
	1374	20	0	0.2150	0.0168	0.2540	0.0076	0.0130	---	0.2310	0.0063	0.2460	
	1379	10	30	0.0982	0.0252	0.1070	0.0128	0.0328	0.1060	0.1300	0.0112	0.1160	
	1380	10	60	0.0673	0.0269	0.0520	0.0218	0.0710	0.1230	0.0900	0.0129	0.0640	
	1381*	10	90	0.0493	0.0407	0.0270	0.0520	0.1080	0.1080	0.0485	0.0300	0.0260	
	1386*	20	180	---	0.2230	0.0085	0.1950	---	---	---	0.2340	---	
100-in. (F) ↓	585	0	0	0.0473	0.0367	0.0234					0.0219	0.0216	0.0235
	590	0	0	0.0516	0.0401	---					0.0233	0.0230	0.0244
	592	0	0	0.0494	0.0389	0.0235					0.0222	0.0220	0.0224
	593	0	0	0.0493	---	0.0236					0.0219	0.0215	0.0220

*These data presented in Ref. 7 also.

TABLE II
TEST CONDITIONS FOR AEDC-VKF PRESSURE DISTRIBUTION DATA
(TEST GAS: NITROGEN)

Tunnel Run No.	Angle of Attack, deg	P_o , psia	T_o , °K	M_∞	Re_∞ /in.	$P_\infty \times 10^3$, psia	T_∞ , °K	q_∞ , psia	U_∞ , fps	P_o , psia
50-in. (H)										
1362	0	7,288	3830	18.42	9,035	1.53	66.74	0.363	10,066	0.678
1363	0	6,229	3498	20.97	6,538	0.57	46.82	0.176	9,597	0.328
1364	0	7,356	3247	18.84	12,464	1.47	53.37	0.366	9,206	0.682
1365	5	6,497	3243	18.79	11,183	1.33	53.59	0.330	9,198	0.614
1366	5	5,803	3460	21.76	5,701	0.43	43.31	0.141	9,577	0.264
1367	10	6,989	3897	18.45	8,313	1.44	67.80	0.342	10,162	0.640
1368	10	6,937	4164	21.57	4,526	0.47	53.82	0.154	10,582	0.289
1369	5	6,609	4561	21.25	3,658	0.47	61.00	0.148	11,098	0.279
1370	0	6,807	2862	19.41	14,274	1.23	44.05	0.324	8,614	0.602
1372	10	8,519	3345	18.97	13,140	1.59	54.44	0.400	9,363	0.746
1373	20	7,263	3376	18.67	11,542	1.51	56.65	0.367	9,400	0.685
1374	20	7,437	3865	18.38	9,082	1.57	67.71	0.372	10,116	0.695
1379	10	6,543	3473	18.99	9,320	1.19	56.47	0.300	9,547	0.560
1380	10	6,519	2890	19.37	13,433	1.18	44.64	0.310	8,655	0.577
1381	10	6,878	3315	18.89	11,046	1.34	54.30	0.334	9,309	0.622
1386	20	7,523	3232	18.94	12,680	1.46	52.58	0.366	9,185	0.682
100-in. (F)										
585	0	19,200	2240	19.40	71,200	4.00	33.62	1.099	7,682	2.044
590	0	22,100	2100	20.10	87,700	4.00	29.81	1.164	7,451	2.164
592	0	22,300	2450	19.30	68,500	4.50	37.27	1.233	8,082	2.295
593	0	21,700	2480	19.20	66,600	4.59	38.22	1.235	8,112	2.300

TABLE III
MODIFIED * PRESSURE DATA FROM CAL 48-IN. SHOCK TUNNEL (REF. 8)

Surface Distance, s Axial Distance, Z _B Model Radial Angle, θ_R , deg			0	1.045	3.510	4.625	4.625	6.890	9.140	9.140	11.390	13.630	13.630	15.890
			-1.00	-0.50	1.940	3.025	3.025	5.250	7.500	7.500	9.720	11.925	11.925	14.130
			---	180	180	0	90	180	0	90	180	0	90	180
Tunnel Run No.	Tunnel Angle of Attack, deg	Tunnel Roll Angle, deg	P/P ₀											
30	0	0	1.000	0.2398	0.0437	0.0373	0.0256	0.0343	0.0330	0.0436	0.0272	0.0316	0.0260	---
31	0	0	1.000	0.2318	0.0396	0.0278	0.0411	---	0.0331	0.0275	0.0192	0.0312	0.0261	0.0194
32	0	0	1.000	0.3300	0.0294	0.0295	---	0.0311	0.0312	0.0254	0.0246	0.0204	0.0258	---
33	0	0	1.000	0.3410	0.0414	0.0296	0.0392	0.0323	0.0325	0.0257	0.0258	0.0293	0.0267	0.0279
12	0	0	1.000	0.2400	0.0450	0.0430	0.0435	0.0352	0.0316	0.0297	0.0276	0.0333	0.0281	0.0307
13	5	0	0.9920	0.1787	0.0321	0.0590	0.0408	0.0231	0.0613	0.0292	0.0163	0.0753	0.0279	0.0160
14	10	0	0.9700	0.1370	0.0246	0.0898	0.0398	0.0189	0.1281	0.0290	0.0130	0.1526	0.0297	0.0124
15	20	0	0.8830	0.0798	0.0183	0.2740	0.0469	0.0154	0.3120	0.0398	0.0100	0.3170	0.0447	0.0083
17	5	180	0.9920	0.2800	0.0591	0.0325	0.0410	0.0540	0.0215	0.0284	0.0562	0.0206	0.0265	0.0732
18	20	180	0.8830	0.1610	0.1890	0.0189	0.0391	0.2393	0.0143	0.0327	0.2297	0.0108	0.0367	0.2410
19	10	180	0.9700	0.3390	0.0750	0.0246	0.0374	0.0936	0.0186	0.0263	0.1118	0.0163	0.0273	0.1345
21	10	90	0.9700	0.2760	0.0540	0.0499	---	0.0540	0.0419	---	0.0363	0.0386	---	0.0384
22	20	90	0.8830	0.2490	0.0549	0.0519	---	0.0502	0.0185	---	0.0476	0.0501	---	0.0481
24	20	180	0.8830	0.5920	0.2420	0.0221	---	0.4019	0.0155	---	0.2860	0.0106	---	0.2930

*See Section 2.2.

TABLE IV
TEST CONDITIONS FOR CAL PRESSURE DISTRIBUTION DATA (REF. 8)
(TEST GAS: AIR)

Tunnel Run No.	Angle of Attack, deg	p_o , psia	$H_o \times 10^{-5}$, ft ² /sec ²	M_∞	Re_∞ /in.	$p_\infty \times 10^3$, psia	T_∞ , °K	q_∞ , psia	U_∞ , fps	p_o^* , psia	p_o^{**} , psia
30	0	2510	36.1	11.65	11,583	2.84	136.9	0.4264	8401	0.7965	0.7434
31	0	1170	36.0	14.35	5,667	1.50	142.0	0.2155	8381	0.4026	0.3474
32	0	623	36.2	14.00	3,083	0.92	150.1	0.1256	8407	0.2346	0.2180
33	0	1177	35.9	14.37	5,667	1.49	141.1	0.2159	8366	0.4033	0.3645
12	0	3903	37.5	13.18	19,250	7.54	167.0	0.9587	8538	1.7917	1.5261
13	5	3923	37.6	13.17	19,250	7.59	167.9	0.9641	8553	1.8019	1.6090
14	10	3905	37.7	13.46	19,083	7.57	168.7	0.9601	8569	1.7945	1.6830
15	20	3973	37.9	13.45	19,250	7.72	169.6	0.9770	8584	1.8262	1.6350
17	5	4005	38.1	13.43	19,167	7.81	171.3	0.9863	8614	1.8437	1.6510
18	20	4073	38.0	13.44	19,667	7.93	170.4	1.0032	8599	1.8751	1.7400
19	10	3737	37.5	13.40	18,500	7.23	167.0	0.9191	8538	1.7176	1.6170
21	10	4030	38.6	13.42	18,917	7.83	173.4	0.9867	8661	1.8447	1.2950
22	20	3975	38.7	13.41	18,500	7.74	174.3	0.9737	8676	1.8205	1.3850
24	20	3890	38.1	13.45	18,583	7.52	170.8	0.9518	8615	1.7792	1.3730



TABLE V
EXPERIMENTAL FORCE COEFFICIENTS AND FREE-STREAM CONDITIONS

Source [†]	Tunnel Run No.	Angle of Attack, deg	C_A	C_N	C_M	p_∞ , psia	T_∞ , °K	M_∞	R_{t_∞} /in.	$p_\infty \times 10^3$, psia	T_∞ , °K	q_∞ , psia	U_∞ , psia	p_∞ , psia
CAL	74	0	0.175	---	---	3492	36.9*	11.75	13,666	3.69	138.1	0.563	8495	1.051
100-in. (F)	79	0	0.160	---	---	7744	3650	19.1	9,250	1.19	57	0.311	9800	0.580
50-in. (H)	1229	5	0.195	0.110	-0.180	6969	3189	18.15	13,118	1.64	55	0.390	9115	0.727
CAL	68	5	0.190	0.114	-0.175	3683	37.2*	14.73	14,250	3.91	139.5	0.594	8526	1.110
CAL	70	10	0.214	0.272	-0.422	3806	37.6*	14.71	14,417	4.04	141.4	0.612	8572	1.143
100 in. (F)	80	10	0.215	0.271	-0.430	7137	3450	19.7	9,350	1.00	52	0.273	9500	0.510
100-in. (F)	82	15	0.261	0.448	-0.684	7943	3700	19.1	9,000	1.24	60	0.323	9900	0.603
100-in. (F)	443	15	0.243	0.465	-0.665	9747	2566	16.5	11,292	5.63	51	1.071	8082	2.000
CAL	71	20	0.283	0.645	-0.981	3592	36.7*	14.77	14,250	3.79	136.7	0.578	8464	1.080
100-in. (F)	89	20	0.304	0.661	-0.976	7474	3350	20.0	10,450	1.08	50	0.284	9400	0.530

* I_a was not given, $H_a \times 10^{-6}$ in H^2/sec^2 was listed.

[†]See also Ref. 7 for AEDC-VKF 100-in. Tunnel F and 50 in. Tunnel H and Ref. 8 for CAL data.

TABLE VI
COMPUTED FORCE AND MOMENT COEFFICIENTS ($\gamma = 1.4$)

Source of Surface Pressure Distribution	Angle of Attack, deg	C_A	C_N	C_m	L/D	C_{N_α}/deg	C_{m_α}/deg
GASL 	0	0.1120	0	0	0	0.01620	-0.02359
	5	0.1182	0.0905	-0.1337	0.635	0.02404	-0.03731
	10	0.1399	0.2452	-0.3761	1.204	0.03465	-0.05073
	15	0.1614	0.4284	-0.6294	1.360	---	---
	20	0.1976	0.6161	-0.9075	1.290	---	---
Modified Newtonian 	0	0.1259	0	0	0	0.03042	-0.03969
	5	0.1308	0.1515	-0.2159	0.972	0.02970	-0.04128
	10	0.1453	0.2982	-0.4255	1.377	0.02970	-0.04199
	15	0.1663	0.4520	-0.6473	1.418	---	---
	20	0.1901	0.6236	-0.8980	1.329	---	---

DOCUMENT CONTROL DATA - R&D

(Security classification of title, body of abstract and indexing annotation must be entered when the overall report is classified)

1 ORIGINATING ACTIVITY (Corporate author) Arnold Engineering Development Center, ARO, Inc., Operating Contractor, Arnold Air Force Station, Tennessee		2a REPORT SECURITY CLASSIFICATION UNCLASSIFIED	
		2b GROUP N/A	
3 REPORT TITLE A COMPARISON OF EXPERIMENTAL AND THEORETICALLY PREDICTED PRESSURE DISTRIBUTIONS AND FORCE AND STABILITY COEFFICIENTS FOR A SPHERICALLY BLUNTED CONE AT $M_{\infty} \sim 18$ AND ANGLES OF ATTACK			
4 DESCRIPTIVE NOTES (Type of report and inclusive dates) N/A			
5. AUTHOR(S) (Last name, first name, initial) Knox, Eugene C., and Lewis, Clark H., ARO, Inc.			
6. REPORT DATE February 1966	7a. TOTAL NO. OF PAGES 61	7b. NO. OF REFS 12	
8a. CONTRACT OR GRANT NO. AF40(600)-1200	9a. ORIGINATOR'S REPORT NUMBER(S) AEDC-TR-65-234		
b. PROJECT NO. 8953			
c. Program Element 62405334	9b. OTHER REPORT NO(S) (Any other numbers that may be assigned this report)		
d. Task 895303	N/A		
10. AVAILABILITY/LIMITATION NOTICES Qualified requesters may obtain copies of this report from DDC. Distribution of this document is unlimited.			
11. SUPPLEMENTARY NOTES N/A		12. SPONSORING MILITARY ACTIVITY Arnold Engineering Development Center, Air Force Systems Command, Arnold Air Force Station, Tennessee	
13 ABSTRACT Analysis of experimental pressure distributions and force and moment coefficients for a 9-deg half-angle spherically blunted cone at $M_{\infty} \sim 18$ and $\alpha = 0$ to 20 deg is presented based on an ideal gas ($\gamma = 1.4$) three-dimensional characteristics solution developed by General Applied Sciences Laboratory (GASL). Comparisons are also made with predictions based on modified Newtonian theory. Pressure distributions along the windward and leeward streamlines were well predicted by the results from the GASL program at $\alpha \approx 10$ deg. For $\alpha < 10$ deg, comparison with the experimental data indicated differences attributed to viscous effects. For $\alpha > 10$ deg the numerical results were affected by necessary program modifications on the leeward side. Radial pressure distri- butions along the body surface from the GASL results showed the development of low pressure "wells" in the leeward region at $\alpha \geq 10$ deg. Similar distributions along a constant entropy surface within the inviscid shock layer indicated substan- tial delay in the formation of the low pressure "wells". C_N and C_m were found to be in good agreement with the experimental data when based on the GASL surface pressure distribution. Predicted values of C_A were about 40 percent below the experimental data over the entire range, $\alpha = 0$ to 20 deg, in agreement with a previous Newtonian based analysis. The difference is attributed to the viscous- induced drag increment. Computed slopes, $C_{N_{\alpha}}$ and $C_{m_{\alpha}}$, were found to be well predicted by the integrated GASL results, whereas the modified Newtonian pre- diction was in poorer agreement with the trends of the experimental data.			

14 KEY WORDS	LINK A		LINK B		LINK C	
	ROLE	WT	ROLE	WT	ROLE	WT
blunted cones						
pressure distributions						
force coefficients						
stability coefficients						
hypersonic flow						
3D characteristics solutions						
angles of attack						
inviscid flow fields						

INSTRUCTIONS

1. **ORIGINATING ACTIVITY:** Enter the name and address of the contractor, subcontractor, grantee, Department of Defense activity or other organization (corporate author) issuing the report.

2a. **REPORT SECURITY CLASSIFICATION:** Enter the overall security classification of the report. Indicate whether "Restricted Data" is included. Marking is to be in accordance with appropriate security regulations.

2b. **GROUP:** Automatic downgrading is specified in DoD Directive 5200.10 and Armed Forces Industrial Manual. Enter the group number. Also, when applicable, show that optional markings have been used for Group 3 and Group 4 as authorized.

3. **REPORT TITLE:** Enter the complete report title in all capital letters. Titles in all cases should be unclassified. If a meaningful title cannot be selected without classification, show title classification in all capitals in parenthesis immediately following the title.

4. **DESCRIPTIVE NOTES:** If appropriate, enter the type of report, e.g., interim, progress, summary, annual, or final. Give the inclusive dates when a specific reporting period is covered.

5. **AUTHOR(S):** Enter the name(s) of author(s) as shown on or in the report. Enter last name, first name, middle initial. If military, show rank and branch of service. The name of the principal author is an absolute minimum requirement.

6. **REPORT DATE:** Enter the date of the report as day, month, year, or month, year. If more than one date appears on the report, use date of publication.

7a. **TOTAL NUMBER OF PAGES:** The total page count should follow normal pagination procedures, i.e., enter the number of pages containing information.

7b. **NUMBER OF REFERENCES:** Enter the total number of references cited in the report.

8a. **CONTRACT OR GRANT NUMBER:** If appropriate, enter the applicable number of the contract or grant under which the report was written.

8b, 8c, & 8d. **PROJECT NUMBER:** Enter the appropriate military department identification, such as project number, subproject number, system numbers, task number, etc.

9a. **ORIGINATOR'S REPORT NUMBER(S):** Enter the official report number by which the document will be identified and controlled by the originating activity. This number must be unique to this report.

9b. **OTHER REPORT NUMBER(S):** If the report has been assigned any other report numbers (either by the originator or by the sponsor), also enter this number(s).

10. **AVAILABILITY/LIMITATION NOTICES:** Enter any limitations on further dissemination of the report, other than those

imposed by security classification, using standard statements such as:

- (1) "Qualified requesters may obtain copies of this report from DDC."
- (2) "Foreign announcement and dissemination of this report by DDC is not authorized."
- (3) "U. S. Government agencies may obtain copies of this report directly from DDC. Other qualified DDC users shall request through _____."
- (4) "U. S. military agencies may obtain copies of this report directly from DDC. Other qualified users shall request through _____."
- (5) "All distribution of this report is controlled. Qualified DDC users shall request through _____."

If the report has been furnished to the Office of Technical Services, Department of Commerce, for sale to the public, indicate this fact and enter the price, if known.

11. **SUPPLEMENTARY NOTES:** Use for additional explanatory notes.

12. **SPONSORING MILITARY ACTIVITY:** Enter the name of the departmental project office or laboratory sponsoring (paying for) the research and development. Include address.

13. **ABSTRACT:** Enter an abstract giving a brief and factual summary of the document indicative of the report, even though it may also appear elsewhere in the body of the technical report. If additional space is required, a continuation sheet shall be attached.

It is highly desirable that the abstract of classified reports be unclassified. Each paragraph of the abstract shall end with an indication of the military security classification of the information in the paragraph, represented as (TS), (S), (C), or (U).

There is no limitation on the length of the abstract. However, the suggested length is from 150 to 225 words.

14. **KEY WORDS:** Key words are technically meaningful terms or short phrases that characterize a report and may be used as index entries for cataloging the report. Key words must be selected so that no security classification is required. Identifiers, such as equipment model designation, trade name, military project code name, geographic location, may be used as key words but will be followed by an indication of technical context. The assignment of links, rules, and weights is optional.